Article

Current Biology

Ultrasonic Neuromodulation via Astrocytic TRPA1

Graphical Abstract

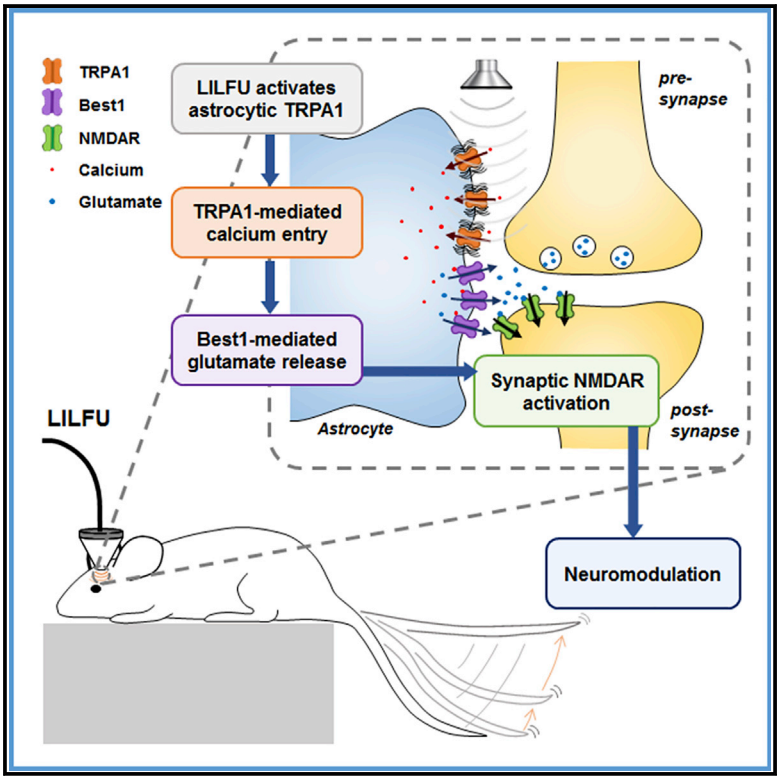

Highlights

- Ultrasound-induced neuromodulation is initiated by opening of TRPA1 in astrocytes
- The Ca^{2+} entry through TRPA1 causes a release of glutamate through Best1 channels
- The released glutamate activates NMDA receptors in neighboring neurons

Authors

Soo-Jin Oh, Jung Moo Lee, Hyun-Bum Kim, ..., Jae Wan Shim, Ji-Ho Park, C. Justin Lee

Correspondence

jae-wan.shim@kist.re.kr (J.W.S.), jihopark@khu.ac.kr (J.-H.P.), cjl@ibs.re.kr (C.J.L.)

In Brief

Oh et al. show that TRPA1 is the molecular sensor and transducer for low-intensity, low-frequency ultrasound (LILFU). With TRPA1's unique co-localization and cooperation with the glutamate-releasing Ca^{2+}-activated Best1 at the microdomains of astrocytes, LILFU is capable of eliciting neuromodulation as a consequence of neuronal NMDAR activation.

Oh et al., 2019, Current Biology *29*, 3386–3401
October 21, 2019
https://doi.org/10.1016/j.cub.2019.08.021

CellPress

CellPress

Current Biology
Article

Ultrasonic Neuromodulation via Astrocytic TRPA1

Soo-Jin Oh,[1,2,14] Jung Moo Lee,[3,4,14] Hyun-Bum Kim,[5,14] Jungpyo Lee,[6,7] Sungmin Han,[8] Jin Young Bae,[9] Gyu-Sang Hong,[1] Wuhyun Koh,[4,10] Jea Kwon,[3,4] Eun-Sang Hwang,[5] Dong Ho Woo,[1] Inchan Youn,[8] Il-Joo Cho,[6,10] Yong Chul Bae,[9] Sungon Lee,[11] Jae Wan Shim,[12,13,*] Ji-Ho Park,[5,*] and C. Justin Lee[1,3,4,10,15,*]

[1]Center for Neuroscience, Korea Institute of Science and Technology (KIST), Seoul 02792, Republic of Korea
[2]Convergence Research Center for Diagnosis, Treatment and Care System of Dementia, Korea Institute of Science and Technology (KIST), Seoul 02792, Republic of Korea
[3]KU-KIST Graduate School of Converging Science and Technology, Korea University, Seoul 02841, Republic of Korea
[4]Center for Cognition and Sociality, Institute for Basic Science, Daejeon 34126, Republic of Korea
[5]Graduate School of East-West Medical Science and Research Institute of Medical Nutrition, Kyung Hee University, Yongin 446-701, Republic of Korea
[6]Center for BioMicrosystems, Korea Institute of Science and Technology (KIST), Seoul 02792, Republic of Korea
[7]Department of Mechanical Engineering, Yonsei University, Seoul 03722, Republic of Korea
[8]Center for Bionics, Korea Institute of Science and Technology (KIST), Seoul 02792, Republic of Korea
[9]Department of Anatomy and Neurobiology, School of Dentistry, Kyungpook National University, Daegu 700-412, Republic of Korea
[10]Division of Bio-Medical Science & Technology, KIST School, Korea University of Science and Technology, Seoul 02792, Republic of Korea
[11]School of Electrical Engineering, Hanyang University, Ansan 15588, Republic of Korea
[12]Materials and Life Science Research Division, Korea Institute of Science and Technology (KIST), Seoul 02792, Republic of Korea
[13]Major of Nanomaterials Science and Engineering, KIST School, Korea University of Science and Technology, Seoul 02792, Republic of Korea
[14]These authors contributed equally
[15]Lead Contact
*Correspondence: jae-wan.shim@kist.re.kr (J.W.S.), jihopark@khu.ac.kr (J.-H.P.), cjl@ibs.re.kr (C.J.L.)
https://doi.org/10.1016/j.cub.2019.08.021

SUMMARY

Low-intensity, low-frequency ultrasound (LILFU) is the next-generation, non-invasive brain stimulation technology for treating various neurological and psychiatric disorders. However, the underlying cellular and molecular mechanism of LILFU-induced neuromodulation has remained unknown. Here, we report that LILFU-induced neuromodulation is initiated by opening of TRPA1 channels in astrocytes. The Ca^{2+} entry through TRPA1 causes a release of gliotransmitters including glutamate through Best1 channels in astrocytes. The released glutamate activates NMDA receptors in neighboring neurons to elicit action potential firing. Our results reveal an unprecedented mechanism of LILFU-induced neuromodulation, involving TRPA1 as a unique sensor for LILFU and glutamate-releasing Best1 as a mediator of glia-neuron interaction. These discoveries should prove to be useful for optimization of human brain stimulation and ultrasonogenetic manipulations of TRPA1.

INTRODUCTION

Neuromodulation is defined as the alteration of neuronal activity through targeted delivery of a stimulus to specific brain regions. Neuromodulation has substantial relevance not only for the treatment of neurological and psychiatric disorders, such as Alzheimer's disease, Parkinson's disease, depression, epilepsy, and chronic pain [1–5], but also for elucidation of how the brain functions during sensory, motor, and cognitive processes. The most commonly employed techniques for neuromodulation and brain stimulation include deep brain stimulation, transcranial magnetic stimulation, transcranial direct current stimulation, and optogenetic and chemogenetic approaches [6]. However, each of these approaches carries serious limitations for human applications. For example, deep brain stimulation requires surgical implantation of stimulating electrode, transcranial magnetic stimulation and transcranial direct current stimulation offer poor spatial resolution, and optogenetic and chemogenetic approaches require genetic manipulations [6].

Low-intensity, low-frequency ultrasound (LILFU) has been considered to be the next-generation, non-invasive brain stimulation technology [7]. The advantages of LILFU have been described [6] as its non-invasive nature, high spatial resolution, deep penetration, combinational use with MRI, cost-effective implementation, and long-lasting neuromodulatory effect without noticeable side effects when the non-thermal power levels range from 30 to 500 mW/cm^2 at the frequency of less than 1 MHz [8]. Reports spanning more than a half century have demonstrated that ultrasound can modulate neuronal activity *in vitro* and *ex vivo* [8, 9]. In recent years, the neuromodulatory effects of LILFU have been reported in multiple animal models *in vivo* [10–13] and in human [14, 15].

Although potential mechanisms underlying ultrasonic neuromodulation have been suggested by many studies [6, 16, 17], the precise cellular target and molecular sensor for LILFU have

remained enigmatic. It has been generally proposed that activation of mechanosensitive channels is one of the potential mechanisms of the ultrasonic neuromodulation. Previous reports describe that Piezo [18], $Na_v1.5$ [19], and K2P, including TREK-1, TREK-2, and TRAAK [19], can be activated by high-intensity, high-frequency ultrasonic stimulation. However, it is unclear whether those mechanosensitive channels (Piezo1, $Na_v1.5$, TREK-1, TREK-2, and TRAAK) can be activated by LILFU. Thus, the search for the identity of LILFU-sensing mechanosensitive channel in the brain continues.

TRPA1, a member of the transient receptor potential (TRP) family, has been actively investigated in the peripheral nociceptor sensory neurons in terms of its function in mechanotransduction [20–23]. In the central nervous system, it has been recently reported that TRPA1 is expressed in astrocytes of the hippocampus, cortex, and trigeminal caudal nucleus [24–29], functioning as a regulator of resting Ca^{2+} level [24, 26]. However, until now, there has been no report about TRPA1 functioning as a sensor for LILFU in the central nervous system. In this study, using the cell-type-specific gene-silencing and ultrasensitive sniffer-patch techniques, we have identified astrocyte as the cellular target and TRPA1 as the molecular sensor for LILFU.

RESULTS

TRPA1 Mediates LILFU-Induced Neuromodulation and Motor Behavior

Transcranial LILFU-stimulated neuronal activity in motor cortex is known to be sufficient to elicit motor behaviors, such as tail movement in mice [12, 30]. As LILFU was shown to induce Ca^{2+} responses in both neurons and astrocytes [8] by exerting a mechanical pressure wave onto plasma membrane, we screened for candidate mechanosensitive Ca^{2+} channels, such as TRPA1 as a molecular target for LILFU-induced neuromodulation. Thus, we first stimulated the motor cortex *in vivo* of wild-type (WT) and TRPA1 knockout (KO) mice by transcranial LILFU (Figure S1) and checked the tail movement score (Figure 1A; Video S1) as previously described [31]. In both WT and TRPA1 KO, tail movement was increased in an intensity-dependent manner (Figure 1B). However, tail movement in TRPA1 KO was significantly reduced compared to WT (Figure 1B), suggesting that TRPA1 mediates LILFU-induced neuromodulation and motor behavior. This difference between WT and TRPA1 KO is not due to an impaired auditory system as recently reported [32, 33], because TRPA1 KO has been demonstrated to be normal in hearing [20].

To determine whether TRPA1 has a critical role in LILFU-stimulated neuronal activity, we measured LILFU-induced neuronal firing in organotypic rat hippocampal slice culture by multielectrode array (MEA) recording (Figures 1C and S2), as we previously reported [9]. We first constructed lentivirus carrying small hairpin-forming interference RNA (shRNA) targeted against TRPA1 (Figures S3D–S3F). Then, we infected the hippocampal CA1 of slice culture with lentivirus carrying control- or TRPA1-shRNA and measured the CA1 pyramidal neuronal activity upon LILFU (Figure 1D). We found that LILFU-induced neuronal firing in TRPA1-shRNA-infected slice was significantly decreased compared to that in control-shRNA-infected slice (Figure 1E). These results indicate that the enhancement of neuronal activity by LILFU could be mediated by TRPA1.

We next asked whether TRPA1 is directly activated by LILFU. We performed Ca^{2+} imaging to measure a LILFU-induced Ca^{2+} increase via TRPA1, which was heterologously expressed in HEK293T. The functional expression of TRPA1 in HEK293T was confirmed by *N*-methylmaleimide (NMM), a TRPA1 selective agonist (Figures S3A–S3C). TRPA1-expressing cells were plated onto a cover glass, which was placed on top of a custom-built piezo-electric micromachined ultrasonic transducer (pMUT) array (Figure 1F), whose physical properties were characterized and described in our previous report [34]. As a result, LILFU-induced Ca^{2+} increase in TRPA1-expressing HEK293T was more frequently observed (Figures 1G and 1H) with significantly higher peak amplitude compared to untransfected control (Figure 1I). These results show that LILFU can open TRPA1 to cause intracellular Ca^{2+} increase.

We next checked other potential molecular sensor for LILFU, such as TRPC1, TRPV4, and Piezo1, by measuring the LILFU-induced Ca^{2+} increase in HEK293T with pMUT array (Figure 2A). We found that LILFU did not induce appreciable Ca^{2+} increase in TRPC1, TRPV4, or Piezo1-expressing HEK293T with significantly lower peak amplitude and percentage of responsive cells than TRPA1-overexpressing HEK293T (Figures 2B and 2C). These results indicate that a well-known mechanosensitive Piezo1 channel and other candidate mechanosensitive TRP channels are not the molecular sensor for LILFU.

LILFU Activates Astrocytic TRPA1 Directly and Neuronal NMDAR Indirectly

To identify the cellular target of LILFU among neurons and astrocytes, we measured LILFU-induced Ca^{2+} increase in the coculture of cortical neurons and astrocytes. We found 42% of responsive cells, including neurons and astrocytes with varying degrees of onset time when we cultured WT neurons and WT astrocytes (Figures 3A–3E). Most of the LILFU-induced Ca^{2+} responses with either fast or slow onset were blocked by HC030031, a selective TRPA1 blocker (Figures 3A–3C). To test whether astrocytic TRPA1 is solely responsible for LILFU-induced Ca^{2+} responses, we substituted WT astrocytes with TRPA1 KO astrocytes, while leaving WT neurons behind. We found a significant reduction of LILFU-induced Ca^{2+} increase with either fast or slow onset in coculture of TRPA1 KO astrocytes and WT neurons (Figures 3A–3C), suggesting that astrocytic TRPA1 is solely responsible for LILFU-induced Ca^{2+} responses. We previously reported that Ca^{2+}-dependent release of glutamate from astrocytes can activate neuronal NDMA receptors (NMDARs) [35–37]. To test whether the LILFU-induced neuronal Ca^{2+} response is mediated by NMDAR, we treated AP-5, an NMDAR selective antagonist, to coculture of WT neurons and WT astrocytes. We found a selective reduction of slow-onset Ca^{2+} responses by AP-5 with only fast-onset Ca^{2+} responses remaining (35%) (Figures 3A–3F). Taken together, these results indicate that LILFU directly targets astrocytic TRPA1, causing the fast-onset Ca^{2+} responses as an upstream signaling to elicit neuronal responses indirectly via NMDARs with the slow-onset Ca^{2+} responses as a downstream signaling of LILFU.

To determine the astrocytic TRPA1 as a sensor for LILFU, we prepared purified cortical astrocyte culture and measured the Ca^{2+} responses induced by NMM or LILFU. We found that

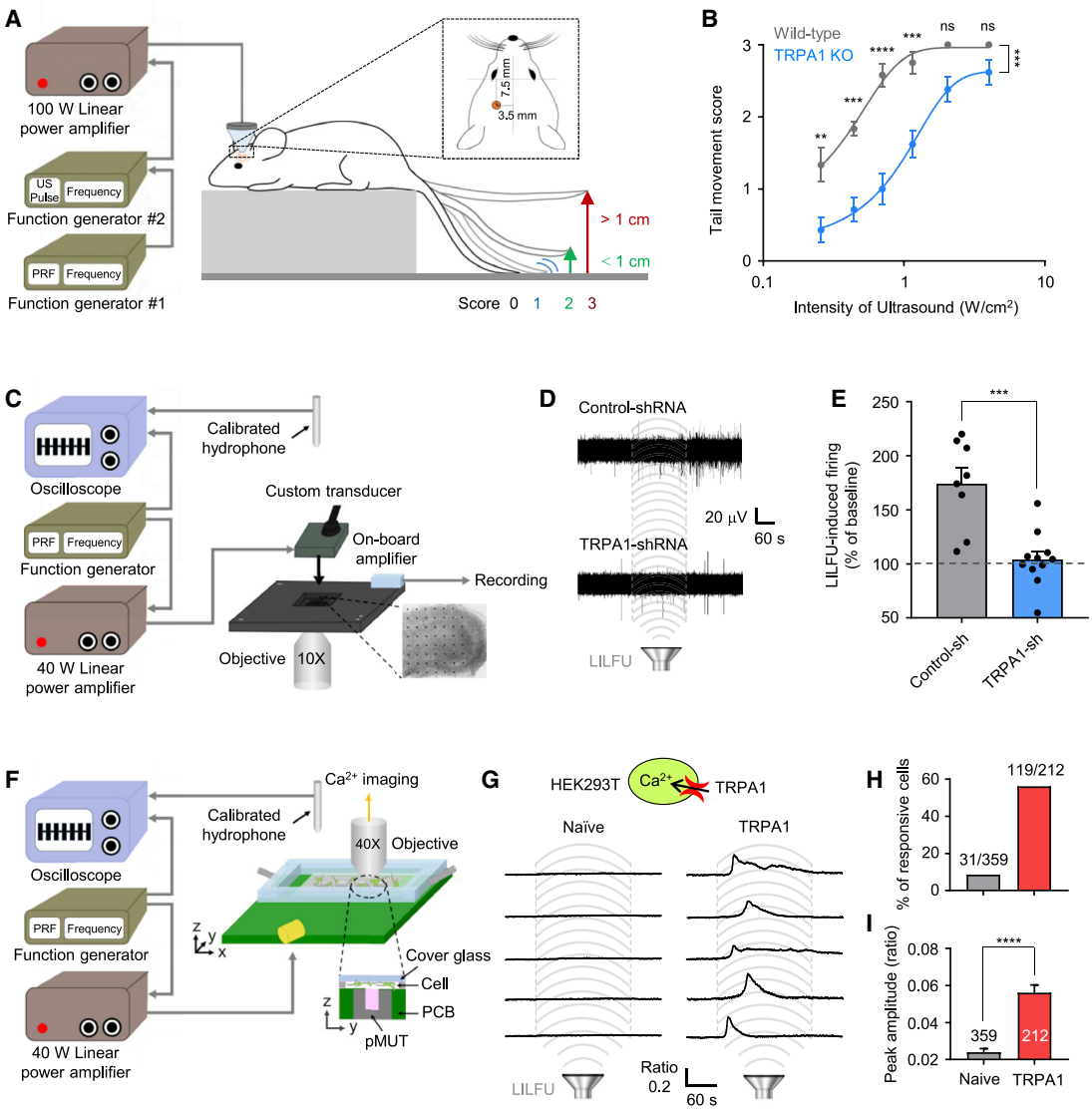

Figure 1. TRPA1 Mediates LILFU-Induced Neuromodulation and Motor Behavior

(A) Schematic diagram of *in vivo* mouse tail movement test using ultrasound to motor cortex.

(B) Tail movement score of WT (n = 4) and TRPA1 KO (n = 7) under various intensities of ultrasound.

(C) Experimental setup of MEA recording with LILFU in organotypic rat hippocampal slice culture. Inset: representative bright field image of hippocampal slice plated on MEA is shown.

(D) Representative traces of LILFU-induced neuronal activity from CA1 region of hippocampal slice infected with control-shRNA (top) and TRPA1-shRNA (bottom).

(E) Summary bar graph showing the number of neuronal firings during 3-min LILFU as a percent of 3-min baseline before LILFU in control- and TRPA1-shRNA-infected slice.

(F) Experimental setup of *in vitro* Ca^{2+} imaging upon LILFU. Inset: pMUT array. PCB, printed circuit board.

(G) Top: schematic diagram of Ca^{2+} imaging from HEK293T. Bottom: representative Ca^{2+} traces of untransfected control and TRPA1-expressing HEK293T upon LILFU.

(H and I) Summary bar graph showing percent of responsive cells (H) and Ca^{2+} peak amplitude (I).

Number on each bar refers to the number of responsive cells over the number of total cells (H) and cells (I) analyzed. Speakers and waves indicate duration of LILFU. Data are presented as mean ± SEM. **p < 0.01; ***p < 0.001; ****p < 0.0001; ns, not significant. Additional statistical details are provided in Table S1. See also Figures S1, S2, and S3 and Video S1.

most of the astrocytes responded to NMM, which was significantly inhibited by expression of TRPA1-shRNA (Figures S3G–S3I), indicating a functional expression of TRPA1 in astrocytes. More importantly, LILFU activated astrocytic TRPA1 by eliciting Ca^{2+} responses with fast onset (Video S2), which was significantly inhibited by HC030031 (Figures 3G–3I) and TRPA1-shRNA (Figures 3J–3L). These results confirm that astrocytic TRPA1 serves as a potential molecular target for LILFU.

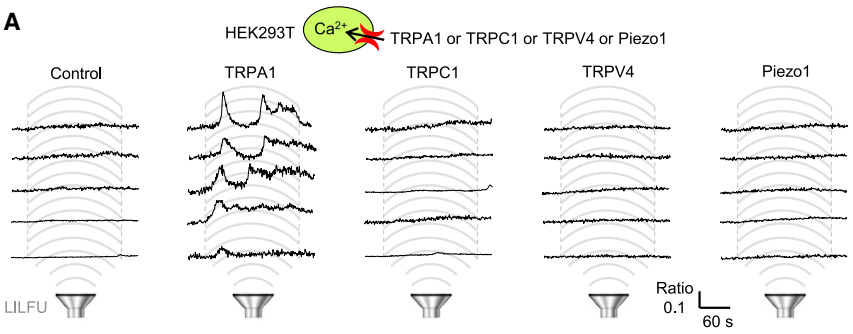

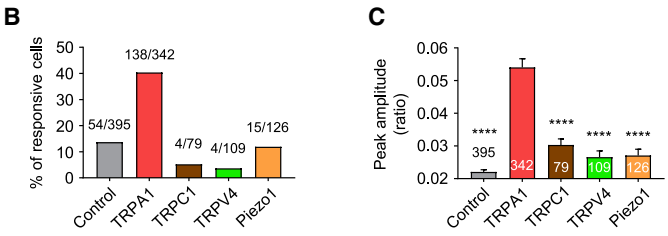

Figure 2. Piezo1 and Other TRPs Do Not Mediate LILFU-Induced Ca^{2+} Increases

(A) Top: schematic diagram of Ca^{2+} imaging from HEK293T. Bottom: Representative Ca^{2+} traces of control vector (pIRES2-EGFP), TRPA1, TRPC1, TRPV4, or Piezo1-expressing HEK293T upon LILFU. (B and C) Summary bar graph showing percent of responsive cells (B) and Ca^{2+} peak amplitude (C). Number on each bar refers to the number of responsive cells over the number of total cells (B) and cells (C) analyzed. Data are presented as mean ± SEM. ****$p < 0.0001$. Additional statistical details are provided in Table S1.
See also Figure S3.

TRPA1, Possibly Activated by Poking, Causes Best1-Mediated Glutamate Release from Astrocyte

To validate whether LILFU-induced Ca^{2+} increase is indeed channel mediated, we tried to directly measure the channel activity by TRPA1 upon LILFU. However, we encountered a difficulty in measuring this current because LILFU disrupted the whole-cell patch clamp. Thus, we changed the stimulation strategy from LILFU to three different modes of mechanical stimulations to mimic the LILFU. First, we tried to perform the piezoelectrically driven fast-exerted mechanical stimulation (600 ms) with varying indentation depths (1, 3, and 5 μm) under whole-cell patch-clamp configuration (Figure 4A) as previously described [38, 39]. We observed fast inactivating mechanosensitive currents upon indentation in 33% of control-vector-expressing HEK293T, which had similar current amplitude and percentage of cells with previous report [38] (Figures 4B and 4C), and no indentation-induced mechanosensitive currents were observed in control-vector-expressing Piezo1 knockout HEK293T (HEK-P1KO) (Figures 4B and 4C), due to an absence of endogenous Piezo1 [38]. In contrast, most of TRPA1-expressing HEK293T did not show any indentation-induced currents (Figures 4B and 4C). Even though 25% of TRPA1-expressing HEK293T showed some distinct non-inactivating currents (Figures 4B, 4D, and 4E), these currents were entirely different from the previously shown Piezo1-expressing HEK293T [38]. These results indicate that mechanical stimulation by fast-exerted indentation is not an optimal mode of mechanical stimulation to activate TRPA1.

As a second mode of mechanical stimulation, we tested a fast-exerted negative pressure (500 ms; 0 to −60 mmHg; Δ10 mmHg) under cell-attached configuration (Figures 4F–4I), as previously described [40]. Unfortunately, we found no sign of negative pressure-induced current upon stimulation (Figures 4G and 4I). Instead, we observed stochastic opening of single-channel currents only in TRPA1-expressing cells (HEK293T or HEK-P1KO), but not in control-vector-expressing cells (Figures 4G and 4I). These single-channel currents were blocked by inclusion of HC030031 in internal solution (Figures 4G and 4I), indicating that these single-channel activities were mediated by TRPA1. Detailed single-channel analyses indicated that these TRPA1-mediated, single-channel activities showed unitary current of 7.48 ± 0.11 pA ($n = 10$) at holding potential of −80 mV, which could be converted to single-channel conductance of 87.7 ± 1.29 pS ($n = 10$). The observed single-channel conductance was similar with previously reported values for TRPA1 [41]. Moreover, the open probability had no significant difference in each negative pressure stimulation condition in HEK293T or HEK-P1KO (Figure 4H), indicating that TRPA1 opens independently of fast-exerted negative pressure. These results indicate that mechanical stimulation by fast-exerted negative pressure is not an optimal mode of mechanical stimulation to activate TRPA1.

Because the fast modes of mechanical stimulation were not effective in activation of TRPA1, we developed and applied a new slow mode of mechanical stimulation of slow-exerted poking with glass pipette (Figures 5A, 5B, and S4C), adopted from our previous report [42]. To perform poking stimulation, we monitored both the indentation depth and the resistance increase (ΔR) of the glass pipette as it touched and pressed the cell membrane with periodic test pulses of 10 mV at 20 Hz (Figures 5A, 5B, and S4A–S4D). We directly measured the current from TRPA1-expressing HEK293T upon poking by performing whole-cell patch clamp (Figure 5C). We found that poking induced a large inward current in 88% of TRPA1-expressing cells, whereas it did not induce any current in control vector or other candidate mechanosensitive TRPs-expressing cells (Figures 5D and 5E). These poking-induced currents were independent of the recently characterized mechanosensitive Ca^{2+} channel Piezo1 [38, 40] (Figures S5A–S5F). To test whether astrocytic TRPA1 can be activated by poking, we measured the poking-induced current from cultured cortical astrocytes (Figure 5F). We discovered that poking elicited large and fast inward currents (average rise time 5.06 ± 0.66 ms; $n = 13$) in control-shRNA-transfected astrocytes, which were almost completely abolished in TRPA1-shRNA-transfected astrocytes (Figures 5G and 5H). Furthermore, opening of TRPA1 by poking caused a robust Ca^{2+} entry in those astrocytes (Figures S5G–S5I). It has been previously reported that *Drosophila* TRPA1 indirectly

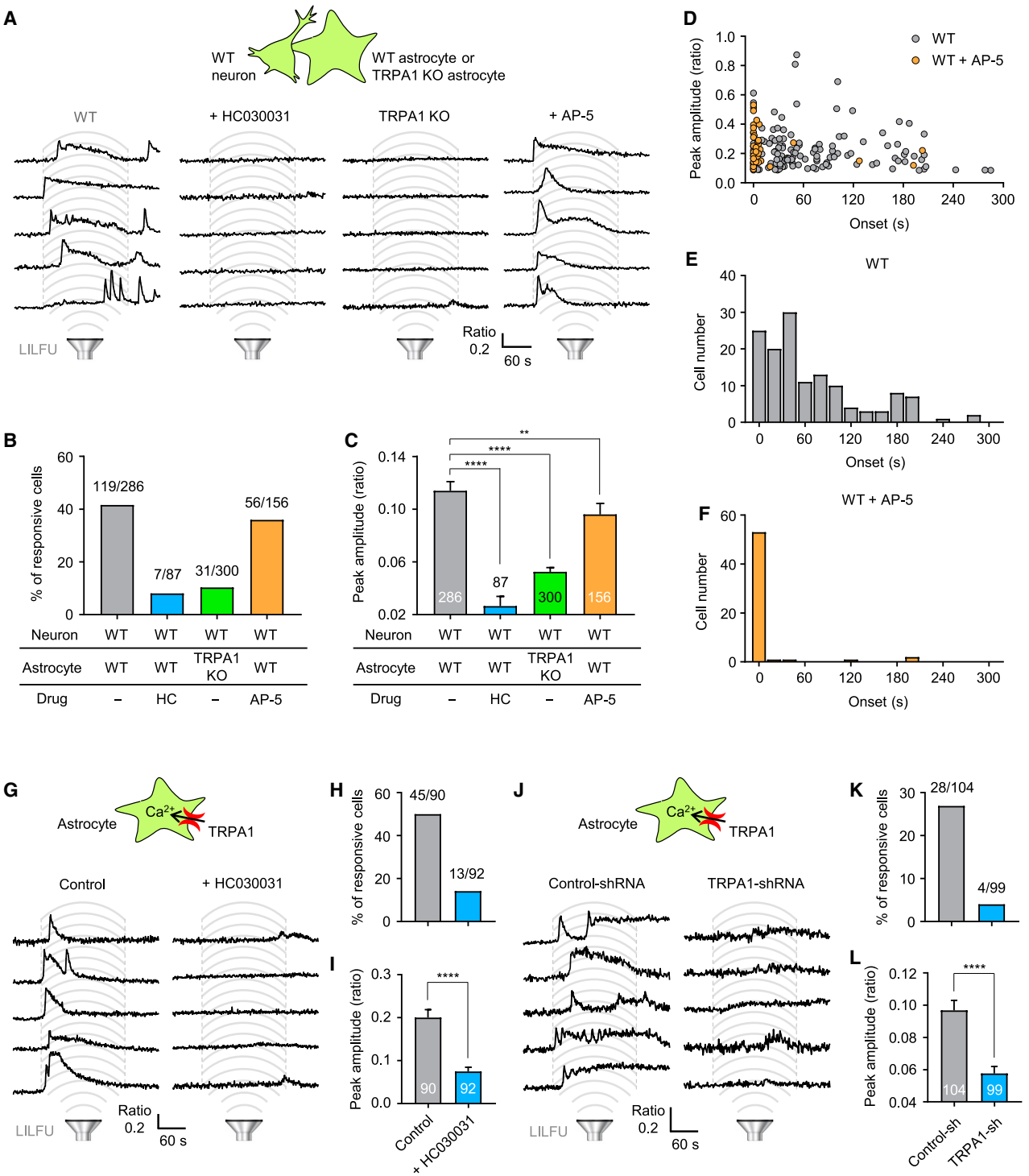

Figure 3. LILFU Activates Astrocytic TRPA1 Directly and Neuronal NMDAR Indirectly

(A) Top: schematic diagram of Ca^{2+} imaging from astrocyte-neuron coculture. Bottom: representative Ca^{2+} traces from WT coculture (WT neurons and WT astrocytes), WT coculture with HC030031 (40 μM) treatment, coculture of WT neurons and TRPA1 KO astrocytes, and WT coculture with AP-5 (50 μM) treatment.

(B) Summary bar graph showing percent of responsive cells.

(C) Summary bar graph of Ca^{2+} peak amplitude.

(D) Plot of Ca^{2+} response onset time versus peak amplitude in WT coculture (gray) and WT coculture with AP-5 (orange).

(E and F) Frequency histogram of the number of responsive cells in WT coculture (E) and WT coculture with AP-5 (F) with 20-s bin of Ca^{2+} response onset time.

(legend continued on next page)

detects UV light by sensing the nucleophiles, such as H_2O_2 [43, 44]. However, our poking-induced responses were not due to indirect activation of TRPA1 through H_2O_2 (Figures S5J–S5L). These results indicate that TRPA1 can be activated by slow-exerted poking as well as LILFU, implying that LILFU can open TRPA1.

We have previously shown that astrocytes can release glutamate upon an increase in intracellular Ca^{2+} concentration through opening of glutamate-permeable, Ca^{2+}-activated anion channel, Best1 [45]. Therefore, to examine whether poking-induced Ca^{2+} entry via TRPA1 causes glutamate release from astrocytes, we performed sniffer-patch technique to detect poking-induced glutamate release from astrocyte with a nearby whole-cell, patch-clamped HEK293T expressing GluR1-L497Y as a biosensor for glutamate (Figure 5I), as previously described [42, 45]. We observed a large poking-induced sensor current from the sensor cell along with a simultaneous Ca^{2+} increase in control-shRNA-transfected astrocyte (Figures 5J–5L). This poking-induced sensor current, as well as poking-induced Ca^{2+} transient, was significantly reduced by TRPA1-shRNA expression in astrocyte (Figures 5J–5L). To test whether poking-induced glutamate release is mediated by Best1, we performed the sniffer patch from Best1-shRNA-transfected astrocytes. We found that sensor current was abolished by Best1-shRNA, and the Ca^{2+} transient was intact in Best1-shRNA-transfected astrocytes (Figures 5J–5L). Taken together, these results show that mechanical stimulation causes Best1-mediated glutamate release from astrocyte and that Ca^{2+} entry via TRPA1 is its upstream signal.

We have utilized poking stimulus to activate the same TRPA1 channel that LILFU targets. However, it has been unclear whether these two seemingly different types of stimuli activate TRPA1 at similar magnitude of pressure. To compare the LILFU- and poking-induced pressure distribution on the surface of astrocyte, we performed computational simulations of 3D astrocytic membrane for LILFU (Figure 5M) and poking stimuli (Figure 5N). The resulting instantaneous 3D surface pressure distribution for LILFU showed a stochastic pressure distribution, which was spread over the whole surface, fluctuating from −30 kPa to +30 kPa (Figure 5M), whereas the result of poking simulation showed a focused pressure distribution around the center of the tip with maximal pressure of 7.2 kPa (Figure 5N). To estimate the threshold pressure for TRPA1 channel activation, we first assumed that poking exerts a local membrane indentation to cause a stretch to the local membrane surface, which results in a maximal activation of nearby TRPA1 channels, as evidenced by a synchronized channel activation with sustained, non-desensitizing kinetics (Figure 5G). In contrast, LILFU exerts instantaneously fluctuating membrane indentations that cause brief TRPA1 channel activations. Based on these assumptions, we compared the average peak Ca^{2+} responses by ultrasound and poking, which were normalized by the NMM-induced Ca^{2+} responses in each recording setup (Figure 5O). This comparison showed that the average LILFU-induced Ca^{2+} response was 33% of the average poking-induced Ca^{2+} response. We then plotted the frequency histogram of pressure distribution of the membrane surface of a single astrocyte by LILFU stimulation (Figure 5P) and identified the minimum pressure value (acoustic power), whose cumulative sum of normalized frequency is 33% of total membrane surface (Figure 5P). We defined this minimal pressure value as the threshold pressure for activation of TRPA1 channel by LILFU and estimated it to be around ±8 kPa (Figure 5P). We made another assumption that astrocytic membrane contains multiple caveoli with membrane invaginations, where TRPA1 channels might be located and anchored to actin filaments perhaps via the ankyrin repeats [46, 47], which can be stretched upon LILFU or poking stimuli to open each channel (Figure S6). It has been previously reported that astrocyte membrane contains caveoli. Each caveolae has a diameter of 80 nm, as previously described for cultured rat cortical astrocyte [48]. In another study, the density of caveoli was 17 per 1 μm^2 in cat optic nerve astrocyte [49]. The membrane stiffness of rat cortical astrocyte has been previously reported to be around 30∼60 kPa at the age of 2∼3 weeks [50]. Using this stiffness value, we simulated the astrocytic surface with 0.75-μm indentation by poking and found the range of pressure to be around 7.2 kPa near the center of the poking area (Figure 5N), where a maximal activation of TRPA1 is induced. This value coincided well within the threshold pressure for channel activation of 8 kPa, which we calculated from the LILFU stimulation. Taken together, the simulation results strongly support the similarity of the estimated pressure for TRPA1 activation between LILFU and poking stimuli.

Released Glutamate from Astrocyte upon LILFU Targets Synaptic NMDAR to Elicit Neuromodulation

Astrocytes make close and intimate contacts with presynaptic and postsynaptic synapses to form the tripartite synapses for bidirectional communication with neighboring neurons [51, 52]. The astrocytic subcellular structure at this tripartite synapse is called microdomain, which consists of a thin and long peripheral process, contacting and wrapping around each synapse [51, 53]. We have previously shown that Best1 is localized in microdomains at synaptic junctions [45, 54] and that Best1-mediated Ca^{2+}-dependent glutamate release specifically targets synaptic NMDAR and modulates synaptic activity [36, 37]. To determine the precise subcellular localization of TRPA1 *in vivo*, we performed an electron microscopic examination of

(G) Top: schematic diagram of Ca^{2+} imaging from cultured cortical astrocytes. Bottom: representative Ca^{2+} traces from naive and HC030031 (40 μM)-treated astrocytes upon LILFU.

(H and I) Summary bar graph showing percent of responsive cells (H) and Ca^{2+} peak amplitude (I).

(J) Top: schematic diagram of Ca^{2+} imaging from cultured cortical astrocytes. Bottom: representative Ca^{2+} traces from control- and TRPA1-shRNA-transfected astrocytes upon LILFU.

(K and L) Summary bar graph showing percent of responsive cells (K) and Ca^{2+} peak amplitude (L).

Number on each bar refers to the number of responsive cells over the number of total cells (B, H, and K) and cells (C, I, and L) analyzed. Data are presented as mean ± SEM. **$p < 0.01$; ****$p < 0.0001$. Additional statistical details are provided in Table S1.

See also Figure S3 and Video S2.

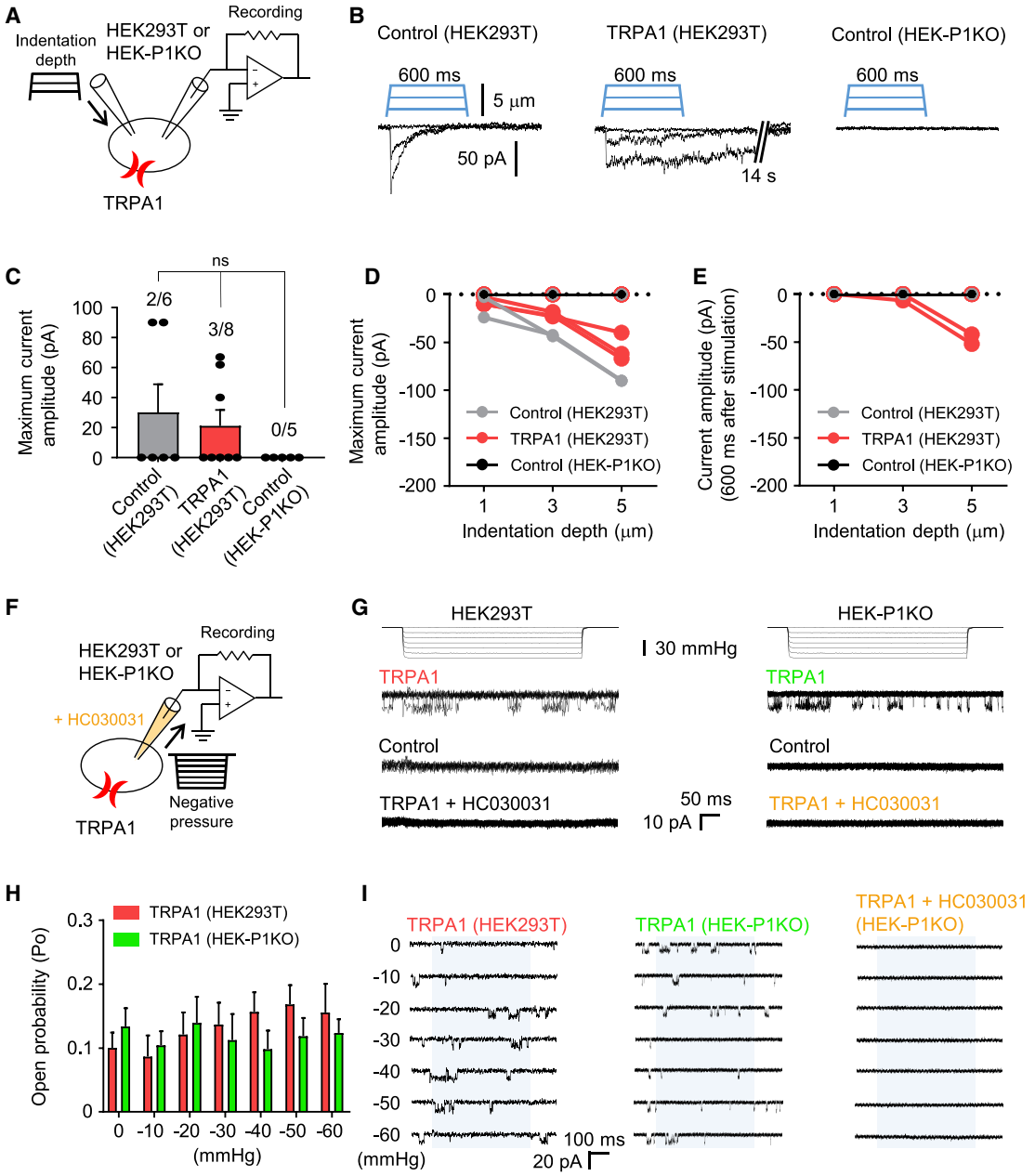

Figure 4. Fast-Exerted Indentation and Negative Pressure Are Not Optimal for TRPA1 Activation

(A) Schematic diagram of whole-cell patch-clamp recording upon fast-exerted indentation (600 ms; 1∼5 μm; Δ2 μm) from HEK293T or HEK293T-Piezo1 knockout (HEK-P1KO).

(B) Representative traces of current recording from control vector (left) or TRPA1 (middle)-expressing HEK293T or control vector-expressing HEK-P1KO (right) upon fast-exerted indentation.

(C) Summary bar graph showing maximum current amplitude.

(D) Summary graph showing maximum current amplitude as a function of stimulus amplitude (indentation depth).

(E) Summary graph showing current amplitude at 600 ms after fast-exerted indentation as a function of stimulus amplitude (indentation depth).

(F) Schematic diagram of cell-attached patch-clamp recording upon fast-exerted negative pressure (500 ms; 0∼−60 mmHg; Δ10 mmHg) from HEK293T or HEK-P1KO.

(G) Left: representative merged traces of current recording from TRPA1-expressing HEK293T with or without HC030031 and control vector-expressing HEK293T upon fast-exerted negative pressure. Right: representative merged traces of channel current recording from TRPA1-expressing HEK-P1KO with or without HC030031 and control vector-expressing HEK-P1KO upon fast-exerted negative pressure.

(H) Summary bar graph showing open probability from TRPA1-expressing HEK293T (n = 10) or HEK-P1KO (n = 8) at each negative pressure.

(legend continued on next page)

immunogold-labeled TRPA1 in immunoperoxidase-labeled GFP-positive profiles in hippocampal CA1 of GFAP-GFP mouse (Figure 6A). We observed that gold particles representing TRPA1 were localized in GFP-positive astrocytes, but not in neurons (Figure 6A). Within an astrocyte, the total number of gold particles for TRPA1 and membrane-bound gold particles for TRPA1 in microdomain were significantly higher than those in soma and process (Figures 6B and 6C). These results indicate that TRPA1 is preferentially localized at microdomains adjacent to synapses where Best1 is also found.

To test whether LILFU-induced glutamate release via Best1 from astrocyte targets synaptic NMDAR to elicit neuronal activity, we measured the LILFU-induced neuronal firing in organotypic rat hippocampal slice culture under various conditions with pharmacological treatments and genetic manipulations (Figures 6D and 6E). We found that TRPA1 blocker (HC030031) and Best1 blockers (niflumic acid and NPPB) abolished LILFU-induced enhancement of neuronal activity (Figure 6E). More importantly, NMDAR blockers (AP-5 and kynurenic acid) eliminated LILFU-induced enhancement of neuronal firing (Figures 6D and 6E). These results indicate that LILFU-induced neuronal activity is mediated by NMDAR. To determine whether astrocytic TRPA1 and Best1 are responsible for LILFU-induced activation of synaptic NMDAR, we performed astrocyte-specific gene silencing [55] of TRPA1 or Best1 (Figure S7A). We infected hippocampal CA1 region of slice culture with lentivirus carrying pSico-TRPA1 or Best1-shRNA-GFP and adeno-associated virus (AAV) carrying GFAP-Cre-mCherry for astrocyte-specific gene silencing of TRPA1 or Best1 (Figure S7B) and then measured the neuronal activity. This astrocyte-specific gene-silencing technique has been extensively tested in our previous paper [56]. We found that gene silencing of TRPA1 or Best1 abolished LILFU-induced enhancement of neuronal firing only when TRPA1-shRNA or Best1-shRNA was combined with AAV carrying GFAP-Cre (Figures 6F and 6G). Finally, we stimulated the mouse motor cortex *in vivo* by transcranial LILFU and tested the tail movement in Best1 KO. As predicted, tail movement by LILFU was dramatically reduced in Best1 KO compared to WT in almost all intensity of LILFU (Figure 6H; Video S3), indicating that Best1 majorly contributes to LILFU-induced neuromodulation. This difference between WT and Best1 KO is not due to impaired auditory system because Best1 KO appears to be normal in hearing. Based on these results, we demonstrate that LILFU activates astrocytic TRPA1 directly and glutamate-releasing Best1 indirectly through Ca^{2+} to target synaptic NMDAR, leading to neuronal firing (Figure 7).

DISCUSSION

To date, previous studies have suggested several mechanisms of neuronal activity induced by non-thermogenic, low-intensity ultrasound. As a possible mechanism of neuromodulation, it has been proposed that the ultrasound causes acoustic cavitation [17] or the formation of gas bubble [57], which could elicit neuronal activity by mechanical forces. However, these proposals have been challenged by the lack of evidence for physical damage or morphological change after LILFU [6]. Another recent report suggested that ultrasonic neuromodulation occurs via mechanical stretch of the lipid bilayer in neurons [8]. However, there has been no direct evidence for the presence of mechanosensitive ion channels in neurons that can be directly activated by LILFU. Surprisingly, we have found the presence of highly sensitive poking-activated channel in astrocytes, but not in neurons, raising astrocytes as the cellular target for LILFU. We have newly characterized the Ca^{2+}-permeable TRPA1 as the specific molecular sensor and transducer for LILFU. With TRPA1's unique co-localization and cooperation with the glutamate-releasing Ca^{2+}-activated Best1 at the microdomains of astrocytes, LILFU is capable of eliciting neuromodulation as a consequence of neuronal NMDAR activation (Figure 7).

Our study is the first to identify the molecular sensor and transducer for LILFU in the mammalian brain. Even though several studies have suggested other mechanosensitive channels, those candidate channels have profoundly different channel properties. For example, Prieto et al. [18] showed that mouse Piezo1 can be activated by ultrasound in Chinese hamster ovary (CHO) or HEK293 cells. However, they observed an activation of Piezo1 by ultrasound stimulation at 43 MHz and 50∼90 W/cm^2. These parameters are far from generally defined LILFU of the non-thermal power levels ranging from 30 to 500 mW/cm^2 at the frequency of less than 1 MHz [8]. We used LILFU at 430 KHz and 306.1 mW/cm^2 for TRPA1 stimulation, which are more than 100-fold different from Piezo1 stimulation. Moreover, we have directly demonstrated that our LILFU stimulation did not cause an appreciable response in Piezo1-expressing HEK293T (Figure 2). Kubanek et al. [19] also showed that $Na_V1.5$ channels and some K2P channels, including TREK-1, TREK-2, and TRAAK, could be activated by focused ultrasound. Again, the authors used focused ultrasound at 10 MHz and 0.3∼4.9 W/cm^2, which are also far from the defined parameters of LILFU. Taken together, we can safely conclude that previously suggested channels are unlikely to be a direct target of LILFU.

Although we have clearly demonstrated that TRPA1 is a sensor for LILFU, whether TRPA1 is a mechanosensitive channel or not is still not clear. It was initially proposed that TRPA1 could be a candidate for the mechanosensitive transduction channel of vertebrate hair cells [58]. However, the same authors disproved their initial claim by demonstrating that TRPA1 is not essential for hair cell transduction but directly or indirectly contributes to the transduction of mechanical stimulus in nociceptor sensory neurons [20]. In more recent reports, it has been shown that indentation-induced, slowly adapting mechanosensitive currents in smaller-diameter dorsal root ganglion (DRG) neurons are absent in TRPA1 KO DRG neurons, indicating that those currents are mediated by TRPA1 [21, 23]. However, both reports did not clearly demonstrate whether TRPA1 is directly activated by

(I) Left: representative traces of current recording from TRPA1-expressing HEK293T at each negative pressure. Middle: representative traces of current recording from TRPA1-expressing HEK-P1KO at each negative pressure. Right: representative traces of current recording from TRPA1-expressing HEK-P1KO with HC030031 in internal solution at each negative pressure. Blue shades indicate the duration of negative pressure (500 ms).
Number on each bar refers to the number of responsive cells over the number of total cells (C). Data are presented as mean ± SEM; ns, not significant. Additional statistical details are provided in Table S1.

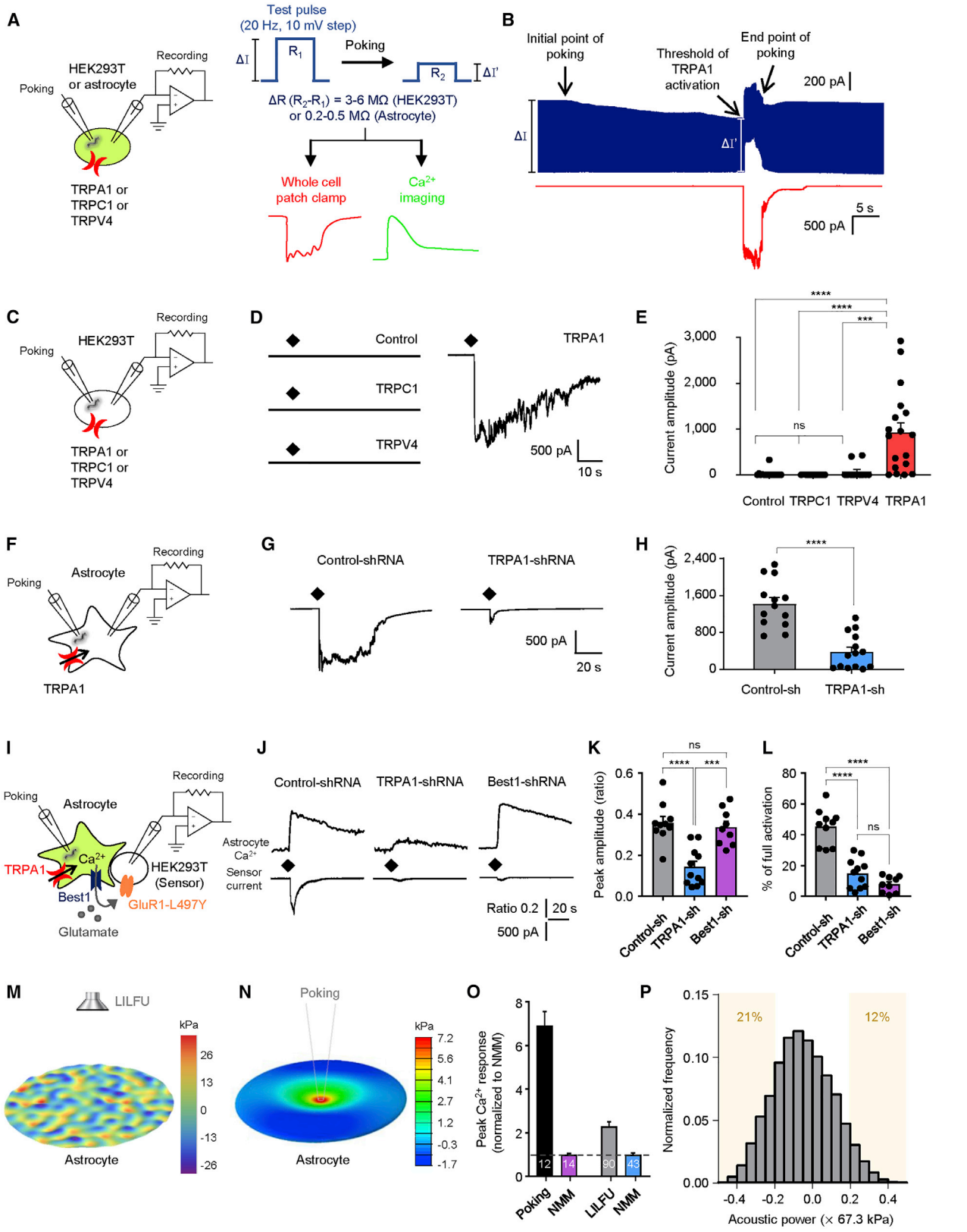

(legend on next page)

membrane stretch or not. Thus, previous claims for TRPA1 as a mechanosensitive channel are still premature. In our current study, we have demonstrated that TRPA1 can be optimally activated by slow-exerted poking stimulation, but not by fast-exerted indentation or negative pressure (Figures 4 and 5A–5L). This provides supporting evidence for a possible activation of TRPA1 by membrane stretch upon slow-exerted poking. Moreover, based on the assumption that TRPA1 is directly activated by poking or LILFU, we performed computational simulations to show that the estimated threshold pressure values for TRPA1 activation by poking and LILFU were similar (Figures 5M–5P). These results imply that our assumption that TRPA1 is directly activated by poking might be correct. Nevertheless, there is still a possibility that TRPA1 could be indirectly activated by unidentified factors upon membrane stretch. Although we have demonstrated that H_2O_2, one of candidate factors for indirect TRPA1 activation, is not involved in our poking-induced TRPA1 activation (Figures S5J–S5L), there might be other unknown factors that need further investigations. For more clear demonstration of TRPA1 as a mechanosensitive channel, future experiments are needed to demonstrate the activity of reconstituted TRPA1 in artificial lipid bilayer upon membrane stretch.

Based on the computational simulations of LILFU and poking stimuli, we have obtained the precise pressure value of 8 kPa, which is required for TRPA1 channel activation upon LILFU stimulation. By obtaining this threshold pressure of TRPA1 channel activation, we have provided supporting evidence for the long-proposed involvement of a mechanosensitive channel and pressure dependence of LILFU-induced neuromodulation [59]. For the possible molecular mechanism of opening of TRPA1 channel by mechanical stimulation, we further hypothesize that pressure exerted on plasma membrane causes the membrane stretch and tension (Figure S6). TRPA1 has long 16∼18 ankyrin repeats in the N-terminal region, which have been hypothesized to tether the channel to cytoskeletal proteins and potentially act as a spring that pulls the channels to open in response to extracellular force, such as mechanical stress [46, 60]. The mechanical displacement of actin filaments during cell stretch might be efficiently increased in the presence of caveolae [61], which are the plasma membrane subdomains of distinct lipid and protein compositions present in many mammalian cells, including astrocytes [48, 49, 62, 63]. It is highly probable that TRPA1 channels might reside in the pit of these caveoli, where the membrane stretch is optimally transduced (Figure S6). Future investigations await for this exciting possibility.

The astrocytic target of LILFU is an unexpected finding, considering the fact that many investigators expected a mechanism involving direct activation of neurons by LILFU [8, 17]. One could still consider a possibility of an off-target effect of LILFU-induced neuromodulation due to an expression of TRPA1 in cell types other than astrocytes in the brain. However, this is unlikely because there are numerous previous reports demonstrating that TRPA1 is specifically expressed in astrocytes and absent in neurons at least within the hippocampus [24, 26]. Consistently, we provide compelling lines of evidence of immunogold electron microscopic results, demonstrating the exclusive expression of TRPA1 in astrocytes, but not in neurons (Figure 6A). Therefore, there should be minimal off-target effect of LILFU-induced neuromodulation at least in the hippocampus, indicating that LILFU-induced neuromodulation is mainly triggered by TRPA1 in astrocytes. Future investigations are needed to establish the cell-type-specific expression pattern of TRPA1 in other brain regions.

One of the most puzzling aspects of LILFU technology is the observed temporal delay for neuro-stimulation by ultrasound [64, 65], which tends to be much slower than electrical and optical stimulation. Consistently, we observed that there is a temporal delay between the onset of LILFU and neuronal responses (Figure S2). Our proposed mechanism can provide a plausible explanation for this puzzle. The proposed model involves a cascade of events that leads to spike firing (Figure 7); LILFU, astrocytic TRPA1 activation (Ca^{2+} increase), Ca^{2+}-dependent Best1 opening (glutamate release), diffusion of glutamate toward neuronal NMDAR, glutamate binding to neuronal NMDAR and relief of Mg^{2+} block, NMDAR channel opening and slow depolarization, and depolarization-induced spike firing. This multistep model contains a couple of steps that might delay the neuronal response time. For example, although TRPA1 activation by

Figure 5. TRPA1, Activated by Poking, Elicits Glutamate Release from Astrocyte via Best1

(A) Schematic diagram showing the method of poking to the cell membrane of HEK293T or astrocyte.

(B) Simultaneous recording of current generated by periodic test pulses of 10 mV at 20 Hz from poking pipette (blue, top) and poking-induced current from recording pipette (red, bottom).

(C) Schematic diagram of whole-cell patch-clamp recording upon poking from HEK293T.

(D) Representative traces of current recording from control vector, TRPA1, TRPC1, or TRPV4-expressing HEK293T transfected with upon poking.

(E) Summary bar graph showing current amplitude.

(F) Schematic diagram of whole-cell patch-clamp recording upon poking from cultured cortical astrocytes.

(G) Representative traces of current recording from astrocytes transfected with control- or TRPA1-shRNA upon poking.

(H) Summary bar graph showing current amplitude.

(I) Schematic diagram of sniffer-patch recording to detect released glutamate.

(J) Representative traces of Ca^{2+} imaging from astrocytes and sniffer current from HEK293T sensor cells upon poking in control-, TRPA1-, or Best1-shRNA-transfected conditions.

(K and L) Summary bar graph of Ca^{2+} peak amplitude from astrocytes (K) and percent of full activation from sensor cells (L).

(M and N) Computational simulation of pressure distribution in 3D astrocytic membrane for LILFU (M) and poking (N) stimuli with lookup table.

(O) Bar graph showing the average peak Ca^{2+} responses upon poking or LILFU. Peak Ca^{2+} responses were normalized by NMM-induced Ca^{2+} responses in each poking or LILFU experimental setup.

(P) The normalized frequency histogram of pressure distribution of the membrane surface of a single astrocyte from (M).

Each diamond indicates time of poking. Data are presented as mean ± SEM. ***$p < 0.001$; ****$p < 0.0001$; ns, not significant. Data are presented as mean ± SEM. Number on each bar refers to the number of cells (O) analyzed. Additional statistical details are provided in Table S1.

See also Figures S4, S5, and S6.

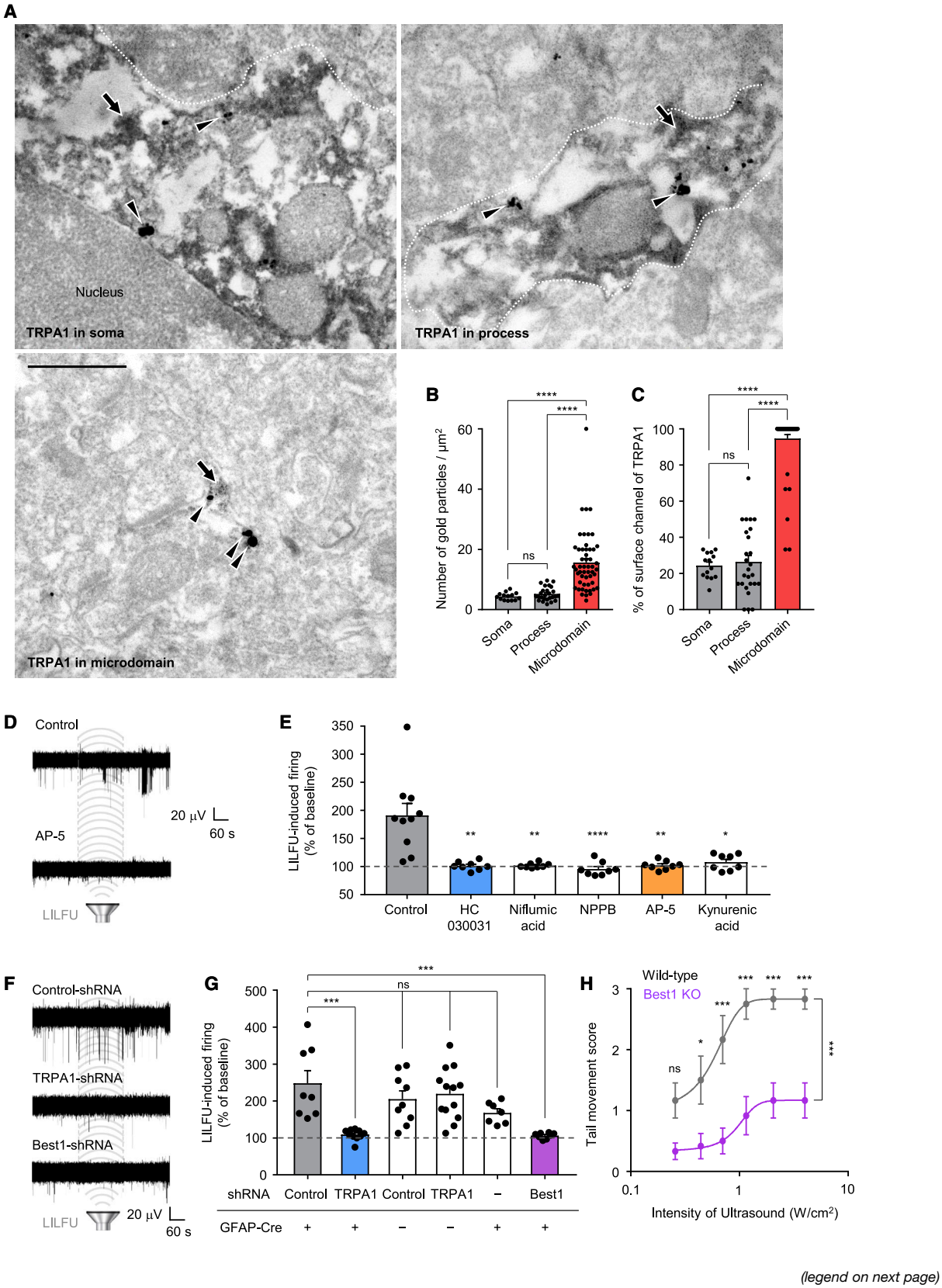

(legend on next page)

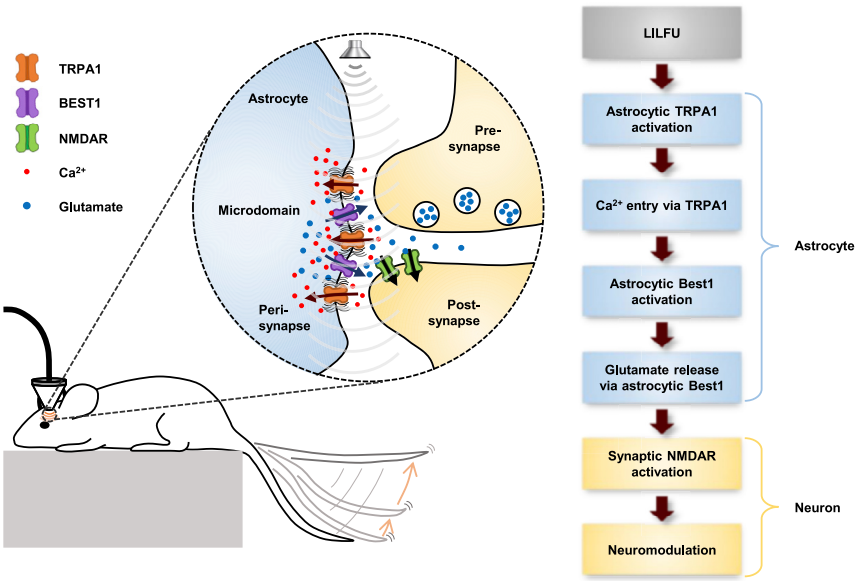

Figure 7. Schematic Model for LILFU-Induced Neuromodulation

LILFU induces Ca^{2+} increase in astrocytes by activation of TRPA1 and glutamate release from astrocytes via Best1. The released glutamate leads to increase of neuronal Ca^{2+} and firing by activating NMDAR, resulting in synaptic plasticity and behavior.

poking is quite fast once it reaches the threshold of membrane stretch or tension (average rise time 5.06 ± 0.66 ms; n = 13; Figure 5G), it takes some time (average onset time for LILFU-induced Ca^{2+} responses: 1.35 ± 0.34 s; n = 53; Figure 3F) for the membrane stretch or tension by LILFU to reach the threshold for channel opening in cultured astrocytes. Another possible time delay could come from the step in which glutamate-bound NMDARs experience the relief of Mg^{2+} block due to a slow regenerative depolarization by its own channel openings. Due to its negative conductance at the negative potentials (below −30 mV) in current-voltage relationship, NMDARs can cause regenerative channel opening and depolarization, similarly to the voltage-gated sodium channels. When neurons are at rest, the resting membrane potential is around −60 mV and the potential needs to reach around −35 mV to initiate an action potential. It would take opening of some number of NMDARs and 100s of millisecond to depolarize from −60 mV to −35 mV. This delay by NMDARs would further slow the spike firing onset time. Taken together, our proposed model is consistent with the observed delay in LILFU-induced neuronal firing.

The preferential activation of NMDAR over other glutamate receptors by LILFU stimulation has been predicted by the estimation of Best1-mediated glutamate release in our previous report. Through diffusion modeling, we previously estimated that glutamate concentration for the slow release through Best1 from a single astrocyte is ~0.9 μM at the target receptor of the opposing neuronal membrane [45]. From this value, we further predicted that glutamate release through Best1 will preferentially activate NMDAR, but not other glutamate receptors, such as AMPAR, mGluR, and KAR, according to the reported concentration-response relationship for each glutamate receptor [45]. Moreover, we have previously demonstrated that Best1-mediated astrocytic glutamate release resulted in activation of GluN2A-containing NMDAR, but not other glutamate receptors, and subsequent NMDAR-dependent potentiation of synaptic responses [37]. Because the concentration of glutamate released through Best1 was much lower (10^{-5}~10^{-6} M) than that from presynaptically released glutamate (~10^{-3} M), this increase in synaptic glutamate levels by Best1 activation had no significant effect on other synaptic glutamate receptors, such as AMPAR and KAR [37]. Therefore, there is a strong possibility that the concentration of released glutamate by LILFU-TRPA1-Best1 pathway may not be sufficient to activate synaptic glutamate receptors other than NMDAR. Finally, it is unlikely that the released glutamate through Best1 activates the synaptic AMPAR, which exhibits rapid and complete desensitization within a few milliseconds when activated by glutamate [66]. Therefore, it is unlikely that other glutamate receptors, such as AMPAR, are directly activated by Best1-mediated glutamate upon LILFU.

We observed the long-lasting Ca^{2+} responses during LILFU stimulation in astrocyte (Figures 3G and 3J). Such

Figure 6. Released Glutamate from Astrocyte upon LILFU Targets Synaptic NMDAR to Elicit Neuromodulation

(A) Electron micrographs showing immunogold staining for TRPA1 in GFAP-GFP mouse hippocampus CA1 region. TRPA1 channels are located in astrocytic soma (top left), process (top right), and microdomain (bottom). Arrowheads indicate TRPA1. Arrows indicate GFP. White dotted lines indicate immunoperoxidase-stained astrocytes. Scale bar, 500 nm.

(B) Summary bar graph showing gold particle density for TRPA1 in soma, process, and microdomain.

(C) Proportion of gold particles located on or near the plasma membrane of the total number of gold particles for TRPA1 in soma, process, and microdomain.

(D) Representative traces of LILFU-induced neuronal firing from CA1 region of control (top) and AP-5 (bottom)-treated hippocampal slice.

(E) Summary bar graph showing the number of neuronal firing during 3-min LILFU as a percent of 3-min baseline before LILFU in control, HC030031 (40 μM), niflumic acid (100 μM), NPPB (100 μM), AP-5 (50 μM), or kynurenic acid (300 μM)-treated slices.

(F) Representative traces of LILFU-induced neuronal activity from CA1 region in control- (top), TRPA1- (middle), or Best1-shRNA (bottom)-infected slice with GFAP-Cre infection.

(G) Summary bar graph showing the number of neuronal firing during 3-min LILFU as a percent of 3-min baseline before LILFU.

(H) Tail movement score of WT (n = 4) and Best1 KO (n = 4) mice under various intensities of ultrasound.

Data are presented as mean ± SEM. *p < 0.05; **p < 0.01; ***p < 0.001; ****p < 0.0001. Additional statistical details are provided in Table S1.

See also Figure S7 and Video S3.

LILFU-induced, long-lasting Ca^{2+} responses could explain the observed long-term effect of ultrasound stimulation, such as alteration of extracellular evoked potentials in the rat dentate gyrus of hippocampus [67], in CA1 of hippocampus [68], and in frog sciatic nerves [69]. In addition, ultrasound stimulation has been shown to increase BDNF protein expression in mouse CA1 and CA3 of hippocampus *in vivo* [12]. We have recently reported that resting astrocytes transform into active astrocytes under the conditions of non-aversive, environmentally beneficial stimulations, such as high neuronal activities or exposure to enriched environment, and that these active astrocytes show enhanced proBDNF expression level [70]. Based on these previous reports, we speculate that LILFU, as an environmentally beneficial stimulation, might transform the resting astrocyte to active astrocyte and enhance expression and release of proBDNF, which is a critical factor for long-term plasticity. This LILFU-induced, BDNF-dependent brain plasticity might require the long-lasting Ca^{2+} responses via astrocytic TRPA1. This exciting possibility needs future investigations.

We hypothesize that our suggested TRPA1-Best1-NMDAR pathway can be expanded beyond the physiological conditions to pathological conditions, such as concussion type of brain injury. Concussion, also known as mild traumatic brain injury, is typically defined as transient neurological dysfunction [71]. Previously, it has been reported that such concussion-type injuries cause a direct mechanical effect on the cells in the brain [72, 73]. These injuries can lead to a cortical spreading depression, which is attributed to massive slow brain depolarizations that interrupt local cortical function for periods of minutes to hours [74, 75]. Astrocytes are known to play an important role in this cortical spreading depression through their propagating Ca^{2+} waves [76, 77]. Based on these previous reports, we predict that the TRPA1-Best1-NMDAR pathway might be an important mechanism involved in initiation and propagation of cortical spreading depression induced by concussion. During concussion, astrocytes can be mechanically stimulated, initiating a cascade of events: hyper-activation of astrocytic TRPA1; increased intracellular Ca^{2+}; excess amount of glutamate release through Best1; over-stimulation of NMDAR; cortical spreading depression; and excitotoxicity. Therefore, the possibility that the TRPA1-Best1-NMDAR pathway might participate in pathophysiological processes, such as brain injury, should be examined in the future.

In addition to the currently popular optogenetics and chemogenetics, the ultrasonogenetics using TRPA1 opens up new avenues for cell-type-specific activation or inhibition and even long-term plasticity when combined with other Ca^{2+}-activated channels or Ca^{2+}-dependent signaling molecules. The insights and tools that we have developed in this study should be useful for future optimization of LILFU as one of the most non-invasive and low-cost neuromodulatory methods for human.

STAR★METHODS

Detailed methods are provided in the online version of this paper and include the following:

- KEY RESOURCES TABLE
- LEAD CONTACT AND MATERIALS AVAILABILITY
- EXPERIMENTAL MODEL AND SUBJECT DETAILS
  - Animals and housing
  - Organotypic hippocampal slice culture preparation
  - HEK293T and HEK293T-Piezo1 knockout (HEK-P1KO) cell culture
  - Primary mouse astrocyte culture
  - Astrocyte-neuron coculture
- METHOD DETAILS
  - Tail movement test with ultrasound
  - Multielectrode array recording of LILFU-induced neuronal firing
  - Micromachined ultrasound transducer array for *in vitro* Ca^{2+} imaging
  - TRP gene cloning and shRNA vector construction
  - Ca^{2+} imaging
  - Indentation (Piezo-electrically driven mechanical stimulation)
  - Poking
  - Whole-cell patch-clamp recording
  - Cell-attached patch-clamp recording with negative pressure
  - Sniffer-patch from primary cultured cortical astrocytes
  - Computational simulation for LILFU- and poking-induced pressure distribution on the surface of astrocyte
  - Electron microscopy
  - Evaluation of mouse skull effect on ultrasound transmission
  - Quantitative real-time PCR
  - Western blot
- QUANTIFICATION AND STATISTICAL ANALYSIS
- DATA AND CODE AVAILABILITY

SUPPLEMENTAL INFORMATION

Supplemental Information can be found online at https://doi.org/10.1016/j.cub.2019.08.021.

ACKNOWLEDGMENTS

This work was supported by grants from National Council of Science & Technology (NST) of Korea (no. CRC-15-04-KIST); National Research Foundation (NRF) of Korea (NRF-2018M3C7A1056897); KBRI basic research program through Korea Brain Research Institute funded by Ministry of Science and ICT (18-BR-03-02); and Institute for Basic Science (IBS), Center for Cognition and Society (IBS-R001-D2).

AUTHOR CONTRIBUTIONS

S.-J.O., H.-B.K., J.-H.P., and C.J.L. designed the experiments. S.-J.O., J.M.L., and C.J.L. wrote the paper. All authors reviewed and edited the manuscript. S.-J.O. and D.H.W. performed and analyzed *in vitro* Ca^{2+} imaging upon LILFU. S.-J.O. also performed and analyzed western blot. J.M.L. performed and analyzed *in vitro* Ca^{2+} imaging, whole-cell patch clamp, and sniffer patch upon poking and performed and analyzed cell-attached patch-clamp recording upon negative pressure. H.-B.K. and E.-S.H. performed and analyzed MEA recording of LILFU-induced neuronal firing. S.L. provided MEA. J.L. and I.-J.C. provided micromachined ultrasound transducer array for *in vitro* Ca^{2+} imaging. S.H. and I.Y. performed and analyzed *in vivo* tail movement test with LILFU. J.W.S. designed the computational simulations and wrote a part of the method related to the computational simulations and performed the mathematical analysis and the simulation of LILFU-induced pressure distribution. J.Y.B. and Y.C.B. performed and analyzed electron

microscopy. G.-S.H. performed and analyzed whole-cell path-clamp recording upon indentation. W.K. performed and analyzed quantitative real-time PCR. J.K. analyzed threshold of *in vitro* Ca^{2+} imaging upon LILFU.

DECLARATION OF INTERESTS

The authors declare no competing interests.

Received: July 11, 2019
Revised: July 26, 2019
Accepted: August 8, 2019
Published: October 3, 2019

REFERENCES

1. Bronstein, J.M., Tagliati, M., Alterman, R.L., Lozano, A.M., Volkmann, J., Stefani, A., Horak, F.B., Okun, M.S., Foote, K.D., Krack, P., et al. (2011). Deep brain stimulation for Parkinson disease: an expert consensus and review of key issues. Arch. Neurol. *68*, 165.
2. Sharma, M., Deogaonkar, M., and Rezai, A. (2015). Assessment of potential targets for deep brain stimulation in patients with Alzheimer's disease. J. Clin. Med. Res. *7*, 501–505.
3. George, M.S., Nahas, Z., Borckardt, J.J., Anderson, B., Burns, C., Kose, S., and Short, E.B. (2007). Vagus nerve stimulation for the treatment of depression and other neuropsychiatric disorders. Expert Rev. Neurother. *7*, 63–74.
4. Al-Otaibi, F.A., Hamani, C., and Lozano, A.M. (2011). Neuromodulation in epilepsy. Neurosurgery *69*, 957–979, discussion 979.
5. Tyler, W.J., Tufail, Y., and Pati, S. (2010). Pain: noninvasive functional neurosurgery using ultrasound. Nat. Rev. Neurol. *6*, 13–14.
6. Bystritsky, A., Korb, A.S., Douglas, P.K., Cohen, M.S., Melega, W.P., Mulgaonkar, A.P., DeSalles, A., Min, B.K., and Yoo, S.S. (2011). A review of low-intensity focused ultrasound pulsation. Brain Stimul. *4*, 125–136.
7. Piper, R.J., Hughes, M.A., Moran, C.M., and Kandasamy, J. (2016). Focused ultrasound as a non-invasive intervention for neurological disease: a review. Br. J. Neurosurg. *30*, 286–293.
8. Tyler, W.J., Tufail, Y., Finsterwald, M., Tauchmann, M.L., Olson, E.J., and Majestic, C. (2008). Remote excitation of neuronal circuits using low-intensity, low-frequency ultrasound. PLoS ONE *3*, e3511.
9. Kim, H.B., Swanberg, K.M., Han, H.S., Kim, J.C., Kim, J.W., Lee, S., Lee, C.J., Maeng, S., Kim, T.S., and Park, J.H. (2017). Prolonged stimulation with low-intensity ultrasound induces delayed increases in spontaneous hippocampal culture spiking activity. J. Neurosci. Res. *95*, 885–896.
10. Kamimura, H.A., Wang, S., Chen, H., Wang, Q., Aurup, C., Acosta, C., Carneiro, A.A., and Konofagou, E.E. (2016). Focused ultrasound neuromodulation of cortical and subcortical brain structures using 1.9 MHz. Med. Phys. *43*, 5730.
11. Deffieux, T., Younan, Y., Wattiez, N., Tanter, M., Pouget, P., and Aubry, J.F. (2013). Low-intensity focused ultrasound modulates monkey visuomotor behavior. Curr. Biol. *23*, 2430–2433.
12. Tufail, Y., Matyushov, A., Baldwin, N., Tauchmann, M.L., Georges, J., Yoshihiro, A., Tillery, S.I., and Tyler, W.J. (2010). Transcranial pulsed ultrasound stimulates intact brain circuits. Neuron *66*, 681–694.
13. Yoo, S.S., Bystritsky, A., Lee, J.H., Zhang, Y., Fischer, K., Min, B.K., McDannold, N.J., Pascual-Leone, A., and Jolesz, F.A. (2011). Focused ultrasound modulates region-specific brain activity. Neuroimage *56*, 1267–1275.
14. Legon, W., Sato, T.F., Opitz, A., Mueller, J., Barbour, A., Williams, A., and Tyler, W.J. (2014). Transcranial focused ultrasound modulates the activity of primary somatosensory cortex in humans. Nat. Neurosci. *17*, 322–329.
15. Hameroff, S., Trakas, M., Duffield, C., Annabi, E., Gerace, M.B., Boyle, P., Lucas, A., Amos, Q., Buadu, A., and Badal, J.J. (2013). Transcranial ultrasound (TUS) effects on mental states: a pilot study. Brain Stimul. *6*, 409–415.
16. Rezayat, E., and Toostani, I.G. (2016). A review on brain stimulation using low intensity focused ultrasound. Basic Clin. Neurosci. *7*, 187–194.
17. Tyler, W.J. (2011). Noninvasive neuromodulation with ultrasound? A continuum mechanics hypothesis. Neuroscientist *17*, 25–36.
18. Prieto, M.L., Firouzi, K., Khuri-Yakub, B.T., and Maduke, M. (2018). Activation of Piezo1 but not $Na_V1.2$ channels by ultrasound at 43 MHz. Ultrasound Med. Biol. *44*, 1217–1232.
19. Kubanek, J., Shi, J., Marsh, J., Chen, D., Deng, C., and Cui, J. (2016). Ultrasound modulates ion channel currents. Sci. Rep. *6*, 24170.
20. Kwan, K.Y., Allchorne, A.J., Vollrath, M.A., Christensen, A.P., Zhang, D.S., Woolf, C.J., and Corey, D.P. (2006). TRPA1 contributes to cold, mechanical, and chemical nociception but is not essential for hair-cell transduction. Neuron *50*, 277–289.
21. Brierley, S.M., Castro, J., Harrington, A.M., Hughes, P.A., Page, A.J., Rychkov, G.Y., and Blackshaw, L.A. (2011). TRPA1 contributes to specific mechanically activated currents and sensory neuron mechanical hypersensitivity. J. Physiol. *589*, 3575–3593.
22. Lennertz, R.C., Kossyreva, E.A., Smith, A.K., and Stucky, C.L. (2012). TRPA1 mediates mechanical sensitization in nociceptors during inflammation. PLoS ONE *7*, e43597.
23. Vilceanu, D., and Stucky, C.L. (2010). TRPA1 mediates mechanical currents in the plasma membrane of mouse sensory neurons. PLoS ONE *5*, e12177.
24. Shigetomi, E., Tong, X., Kwan, K.Y., Corey, D.P., and Khakh, B.S. (2011). TRPA1 channels regulate astrocyte resting calcium and inhibitory synapse efficacy through GAT-3. Nat. Neurosci. *15*, 70–80.
25. Bosson, A., Paumier, A., Boisseau, S., Jacquier-Sarlin, M., Buisson, A., and Albrieux, M. (2017). TRPA1 channels promote astrocytic Ca^{2+} hyperactivity and synaptic dysfunction mediated by oligomeric forms of amyloid-β peptide. Mol. Neurodegener. *12*, 53.
26. Shigetomi, E., Jackson-Weaver, O., Huckstepp, R.T., O'Dell, T.J., and Khakh, B.S. (2013). TRPA1 channels are regulators of astrocyte basal calcium levels and long-term potentiation via constitutive D-serine release. J. Neurosci. *33*, 10143–10153.
27. Lee, S.M., Cho, Y.S., Kim, T.H., Jin, M.U., Ahn, D.K., Noguchi, K., and Bae, Y.C. (2012). An ultrastructural evidence for the expression of transient receptor potential ankyrin 1 (TRPA1) in astrocytes in the rat trigeminal caudal nucleus. J. Chem. Neuroanat. *45*, 45–49.
28. Lee, K.I., Lee, H.T., Lin, H.C., Tsay, H.J., Tsai, F.C., Shyue, S.K., and Lee, T.S. (2016). Role of transient receptor potential ankyrin 1 channels in Alzheimer's disease. J. Neuroinflammation *13*, 92.
29. Jackson, J.G., and Robinson, M.B. (2015). Reciprocal regulation of mitochondrial dynamics and calcium signaling in astrocyte processes. J. Neurosci. *35*, 15199–15213.
30. King, R.L., Brown, J.R., Newsome, W.T., and Pauly, K.B. (2013). Effective parameters for ultrasound-induced in vivo neurostimulation. Ultrasound Med. Biol. *39*, 312–331.
31. Mehić, E., Xu, J.M., Caler, C.J., Coulson, N.K., Moritz, C.T., and Mourad, P.D. (2014). Increased anatomical specificity of neuromodulation via modulated focused ultrasound. PLoS ONE *9*, e86939.
32. Sato, T., Shapiro, M.G., and Tsao, D.Y. (2018). Ultrasonic neuromodulation causes widespread cortical activation via an indirect auditory mechanism. Neuron *98*, 1031–1041.e5.
33. Guo, H., Hamilton Ii, M., Offutt, S.J., Gloeckner, C.D., Li, T., Kim, Y., Legon, W., Alford, J.K., and Lim, H.H. (2018). Ultrasound produces extensive brain activation via a cochlear pathway. Neuron *99*, 866.
34. Lee, J., Ko, K., Shin, H., Oh, S.-J., Lee, C.J., Chou, N., Choi, N., Oh, M.T., Lee, B.C., Jun, S.C., et al. (2019). A MEMS ultrasound stimulation system for modulation of neural circuits with high spatial resolution in vitro. Microsyst. Nanoeng. *5*, 28.
35. Lee, C.J., Mannaioni, G., Yuan, H., Woo, D.H., Gingrich, M.B., and Traynelis, S.F. (2007). Astrocytic control of synaptic NMDA receptors. J. Physiol. *581*, 1057–1081.

36. Han, K.S., Woo, J., Park, H., Yoon, B.J., Choi, S., and Lee, C.J. (2013). Channel-mediated astrocytic glutamate release via Bestrophin-1 targets synaptic NMDARs. Mol. Brain *6*, 4.
37. Park, H., Han, K.S., Seo, J., Lee, J., Dravid, S.M., Woo, J., Chun, H., Cho, S., Bae, J.Y., An, H., et al. (2015). Channel-mediated astrocytic glutamate modulates hippocampal synaptic plasticity by activating postsynaptic NMDA receptors. Mol. Brain *8*, 7.
38. Dubin, A.E., Murthy, S., Lewis, A.H., Brosse, L., Cahalan, S.M., Grandl, J., Coste, B., and Patapoutian, A. (2017). Endogenous Piezo1 can confound mechanically activated channel identification and characterization. Neuron *94*, 266–270.e3.
39. Hong, G.S., Lee, B., Wee, J., Chun, H., Kim, H., Jung, J., Cha, J.Y., Riew, T.R., Kim, G.H., Kim, I.B., and Oh, U. (2016). Tentonin 3/TMEM150c confers distinct mechanosensitive currents in dorsal-root ganglion neurons with proprioceptive function. Neuron *91*, 107–118.
40. Coste, B., Mathur, J., Schmidt, M., Earley, T.J., Ranade, S., Petrus, M.J., Dubin, A.E., and Patapoutian, A. (2010). Piezo1 and Piezo2 are essential components of distinct mechanically activated cation channels. Science *330*, 55–60.
41. Nagata, K., Duggan, A., Kumar, G., and García-Añoveros, J. (2005). Nociceptor and hair cell transducer properties of TRPA1, a channel for pain and hearing. J. Neurosci. *25*, 4052–4061.
42. Lee, J., Chun, Y.E., Han, K.S., Lee, J., Woo, D.H., and Lee, C.J. (2015). Ca(2+) entry is required for mechanical stimulation-induced ATP release from astrocyte. Exp. Neurobiol. *24*, 17–23.
43. Guntur, A.R., Gu, P., Takle, K., Chen, J., Xiang, Y., and Yang, C.H. (2015). Drosophila TRPA1 isoforms detect UV light via photochemical production of H2O2. Proc. Natl. Acad. Sci. USA *112*, E5753–E5761.
44. Du, E.J., Ahn, T.J., Wen, X., Seo, D.W., Na, D.L., Kwon, J.Y., Choi, M., Kim, H.W., Cho, H., and Kang, K. (2016). Nucleophile sensitivity of *Drosophila* TRPA1 underlies light-induced feeding deterrence. eLife *5*, e18425.
45. Woo, D.H., Han, K.S., Shim, J.W., Yoon, B.E., Kim, E., Bae, J.Y., Oh, S.J., Hwang, E.M., Marmorstein, A.D., Bae, Y.C., et al. (2012). TREK-1 and Best1 channels mediate fast and slow glutamate release in astrocytes upon GPCR activation. Cell *151*, 25–40.
46. Howard, J., and Bechstedt, S. (2004). Hypothesis: a helix of ankyrin repeats of the NOMPC-TRP ion channel is the gating spring of mechanoreceptors. Curr. Biol. *14*, R224–R226.
47. Barritt, G., and Rychkov, G. (2005). TRPs as mechanosensitive channels. Nat. Cell Biol. *7*, 105–107.
48. Cameron, P.L., Ruffin, J.W., Bollag, R., Rasmussen, H., and Cameron, R.S. (1997). Identification of caveolin and caveolin-related proteins in the brain. J. Neurosci. *17*, 9520–9535.
49. Massa, P.T. (1982). Plasmalemmal vesicles (caveolae) of fibrous astrocytes of the cat optic nerve. Am. J. Anat. *165*, 69–81.
50. Lee, S.M., Nguyen, T.H., Na, K., Cho, I.J., Woo, D.H., Oh, J.E., Lee, C.J., and Yoon, E.S. (2015). Nanomechanical measurement of astrocyte stiffness correlated with cytoskeletal maturation. J. Biomed. Mater. Res. A *103*, 365–370.
51. Halassa, M.M., Fellin, T., and Haydon, P.G. (2007). The tripartite synapse: roles for gliotransmission in health and disease. Trends Mol. Med. *13*, 54–63.
52. Allen, N.J., and Barres, B.A. (2009). Neuroscience: glia - more than just brain glue. Nature *457*, 675–677.
53. Grosche, J., Matyash, V., Möller, T., Verkhratsky, A., Reichenbach, A., and Kettenmann, H. (1999). Microdomains for neuron-glia interaction: parallel fiber signaling to Bergmann glial cells. Nat. Neurosci. *2*, 139–143.
54. Park, H., Han, K.S., Oh, S.J., Jo, S., Woo, J., Yoon, B.E., and Lee, C.J. (2013). High glutamate permeability and distal localization of Best1 channel in CA1 hippocampal astrocyte. Mol. Brain *6*, 54.
55. Ventura, A., Meissner, A., Dillon, C.P., McManus, M., Sharp, P.A., Van Parijs, L., Jaenisch, R., and Jacks, T. (2004). Cre-lox-regulated conditional RNA interference from transgenes. Proc. Natl. Acad. Sci. USA *101*, 10380–10385.
56. Jung, J.Y., Lee, S.E., Hwang, E.M., and Lee, C.J. (2016). Neuronal expression and cell-type-specific gene-silencing of Best1 in thalamic reticular nucleus neurons using pSico-Red system. Exp. Neurobiol. *25*, 120–129.
57. Bailey, M.R., Dalecki, D., Child, S.Z., Raeman, C.H., Penney, D.P., Blackstock, D.T., and Carstensen, E.L. (1996). Bioeffects of positive and negative acoustic pressures in vivo. J. Acoust. Soc. Am. *100*, 3941–3946.
58. Corey, D.P., García-Añoveros, J., Holt, J.R., Kwan, K.Y., Lin, S.Y., Vollrath, M.A., Amalfitano, A., Cheung, E.L., Derfler, B.H., Duggan, A., et al. (2004). TRPA1 is a candidate for the mechanosensitive transduction channel of vertebrate hair cells. Nature *432*, 723–730.
59. Younan, Y., Deffieux, T., Larrat, B., Fink, M., Tanter, M., and Aubry, J.F. (2013). Influence of the pressure field distribution in transcranial ultrasonic neurostimulation. Med. Phys. *40*, 082902.
60. Sotomayor, M., Corey, D.P., and Schulten, K. (2005). In search of the hair-cell gating spring elastic properties of ankyrin and cadherin repeats. Structure *13*, 669–682.
61. Gervásio, O.L., Phillips, W.D., Cole, L., and Allen, D.G. (2011). Caveolae respond to cell stretch and contribute to stretch-induced signaling. J. Cell Sci. *124*, 3581–3590.
62. Hill, M.M., Bastiani, M., Luetterforst, R., Kirkham, M., Kirkham, A., Nixon, S.J., Walser, P., Abankwa, D., Oorschot, V.M., Martin, S., et al. (2008). PTRF-Cavin, a conserved cytoplasmic protein required for caveola formation and function. Cell *132*, 113–124.
63. Massa, P.T., and Mugnaini, E. (1985). Cell-cell junctional interactions and characteristic plasma membrane features of cultured rat glial cells. Neuroscience *14*, 695–709.
64. Lee, W., Chung, Y.A., Jung, Y., Song, I.U., and Yoo, S.S. (2016). Simultaneous acoustic stimulation of human primary and secondary somatosensory cortices using transcranial focused ultrasound. BMC Neurosci. *17*, 68.
65. Kim, H., Lee, S.D., Chiu, A., Yoo, S.S., and Park, S. (2014). Estimation of the spatial profile of neuromodulation and the temporal latency in motor responses induced by focused ultrasound brain stimulation. Neuroreport *25*, 475–479.
66. Sun, Y., Olson, R., Horning, M., Armstrong, N., Mayer, M., and Gouaux, E. (2002). Mechanism of glutamate receptor desensitization. Nature *417*, 245–253.
67. Bachtold, M.R., Rinaldi, P.C., Jones, J.P., Reines, F., and Price, L.R. (1998). Focused ultrasound modifications of neural circuit activity in a mammalian brain. Ultrasound Med. Biol. *24*, 557–565.
68. Rinaldi, P.C., Jones, J.P., Reines, F., and Price, L.R. (1991). Modification by focused ultrasound pulses of electrically evoked responses from an in vitro hippocampal preparation. Brain Res. *558*, 36–42.
69. Colucci, V., Strichartz, G., Jolesz, F., Vykhodtseva, N., and Hynynen, K. (2009). Focused ultrasound effects on nerve action potential in vitro. Ultrasound Med. Biol. *35*, 1737–1747.
70. Chun, H., An, H., Lim, J., Woo, J., Lee, J., Ryu, H., and Lee, C.J. (2018). Astrocytic proBDNF and tonic GABA distinguish active versus reactive astrocytes in hippocampus. Exp. Neurobiol. *27*, 155–170.
71. Giza, C.C., and Hovda, D.A. (2001). The neurometabolic cascade of concussion. J. Athl. Train. *36*, 228–235.
72. Ward, A.A., Jr. (1958). Physiological basis of concussion. J. Neurosurg. *15*, 129–134.
73. Miller, G.G. (1927). Cerebral concussion. Arch. Surg. *14*, 891–916.
74. Torrente, D., Cabezas, R., Avila, M.F., García-Segura, L.M., Barreto, G.E., and Guedes, R.C. (2014). Cortical spreading depression in traumatic brain injuries: is there a role for astrocytes? Neurosci. Lett. *565*, 2–6.
75. Rovegno, M., and Sáez, J.C. (2018). Role of astrocyte connexin hemichannels in cortical spreading depression. Biochim Biophys Acta Biomembr *1860*, 216–223.
76. Li, B., Chen, S., Zeng, S., Luo, Q., and Li, P. (2012). Modeling the contributions of Ca2+ flows to spontaneous Ca2+ oscillations and cortical spreading depression-triggered Ca2+ waves in astrocyte networks. PLoS ONE *7*, e48534.

77. Enger, R., Tang, W., Vindedal, G.F., Jensen, V., Johannes Helm, P., Sprengel, R., Looger, L.L., and Nagelhus, E.A. (2015). Dynamics of ionic shifts in cortical spreading depression. Cereb. Cortex *25*, 4469–4476.

78. Marmorstein, L.Y., Wu, J., McLaughlin, P., Yocom, J., Karl, M.O., Neussert, R., Wimmers, S., Stanton, J.B., Gregg, R.G., Strauss, O., et al. (2006). The light peak of the electroretinogram is dependent on voltage-gated calcium channels and antagonized by bestrophin (best-1). J. Gen. Physiol. *127*, 577–589.

79. Han, S., Kim, M., Kim, H., Shin, H., and Youn, I. (2018). Ketamine inhibits ultrasound stimulation-induced neuromodulation by blocking cortical neuron activity. Ultrasound Med. Biol. *44*, 635–646.

80. Li, G.F., Zhao, H.X., Zhou, H., Yan, F., Wang, J.Y., Xu, C.X., Wang, C.Z., Niu, L.L., Meng, L., Wu, S., et al. (2016). Improved anatomical specificity of non-invasive neuro-stimulation by high frequency (5 MHz) ultrasound. Sci. Rep. *6*, 24738.

81. Egert, U., Schlosshauer, B., Fennrich, S., Nisch, W., Fejtl, M., Knott, T., Müller, T., and Hämmerle, H. (1998). A novel organotypic long-term culture of the rat hippocampus on substrate-integrated multielectrode arrays. Brain Res. Brain Res. Protoc. *2*, 229–242.

82. Rosin, P.L. (2001). Unimodal thresholding. Pattern Recognit. *34*, 2083–2096.

83. Dai, Y., Wang, S., Tominaga, M., Yamamoto, S., Fukuoka, T., Higashi, T., Kobayashi, K., Obata, K., Yamanaka, H., and Noguchi, K. (2007). Sensitization of TRPA1 by PAR2 contributes to the sensation of inflammatory pain. J. Clin. Invest. *117*, 1979–1987.

84. Tufail, Y., Yoshihiro, A., Pati, S., Li, M.M., and Tyler, W.J. (2011). Ultrasonic neuromodulation by brain stimulation with transcranial ultrasound. Nat. Protoc. *6*, 1453–1470.

STAR★METHODS

KEY RESOURCES TABLE

REAGENT or RESOURCE	SOURCE	IDENTIFIER
Antibodies		
Chicken anti-GFP	Aves Labs	Cat#GFP-1020; RRID: AB_10000240
Rabbit anti-TRPA1	[78]	N/A
Rabbit anti-TRPA1	Abfrontier	N/A
Rabbit anti-actin	Sigma-Aldrich	Cat#A2066; RRID: AB_10013287
Biotin-SP (long spacer) AffiniPure Donkey Anti-Chicken IgY (IgG) (H+L)	Jackson ImmunoResearch	Cat#703-065-155; RRID: AB_2313596
Gold-conjugated Donkey-anti-Rabbit IgG (H&L)	EMS	Cat#25701; RRID: AB_2629850
Horseradish peroxidase-conjugated donkey anti-rabbit IgG	Amersham	Cat#NA9340; RRID: AB_772191
Bacterial and Virus Strains		
pLenti-pSicoR-control-shRNA-GFP	KIST virus facility	N/A
pLenti-pSicoR-mouse TRPA1-shRNA-GFP	KIST virus facility	N/A
pLenti-pSico-control-shRNA-GFP	KIST virus facility	N/A
pLenti-pSico-mouse TRPA1-shRNA-GFP	KIST virus facility	N/A
pLenti-pSico-mouse Best1-shRNA-GFP	KIST virus facility	N/A
AAV-GFAP-Cre-mCherry	KIST virus facility	N/A
Chemicals, Peptides, and Recombinant Proteins		
D-AP5	Tocris	Cat#0106; CAS: 79055-68-8
HC030031	Sigma-Aldrich	Cat#H4415; CAS: 349085-38-7
Thapsigargin	Sigma-Aldrich	Cat#T9033; CAS: 67526-95-8
CNQX	Tocris	Cat#0190; CAS: 115066-14-3
Edaravone (MCI-186)	abcam	Cat#ab120645, CAS: 89-25-8
AAD-2004	GNT Pharma	N/A
Niflumic acid	Sigma-Aldrich	Cat#N0630; CAS: 4394-00-7
5-Nitro-2-(3-phenylpropylamino)benzoic acid (NPPB)	Sigma-Aldrich	Cat#N4779; CAS: 107254-86-4
Kynuranic acid	Sigma-Aldrich	Cat#K3375; CAS: 492-27-3
N-Methylmaleimide	Sigma-Aldrich	Cat#389412; CAS: 930-88-1
Experimental Models: Cell Lines		
Human: HEK293T cells	ATCC	RRID: CVCL_0063
Human: HEK-P1KO cells	[38]	N/A
Experimental Models: Organisms/Strains		
Mouse: C57BL/6J	The Jackson Laboratory	RRID: IMSR_JAX:000664
Mouse: Trpa1 KO: B6;129P-Trpa1^{tm1Kykw}/J	The Jackson Laboratory	RRID: IMSR_JAX:006401
Mouse: Best1 KO: Best1^{tm1Lmar}/Best1^{tm1Lmar}	[79]	RRID: MGI:3797408
Mouse: hGFAP-GFP: FVB/N-Tg(GFAPGFP)14Mes/J	The Jackson Laboratory	RRID: IMSR_JAX:003257
Rat: Sprague-Dawley rats	DBL	N/A
Oligonucleotides		
shRNA targeting sequence: TRPA1: gcaagcttccttt ctgcatat	This paper	N/A
shRNA targeting sequence: Best1: tttgccaacttgtc aatgaa	[45]	N/A
Primer: Mouse TRPA1 Forward: gcatacccagtcct gacctt	This paper	N/A

(*Continued on next page*)

Continued

REAGENT or RESOURCE	SOURCE	IDENTIFIER
Primer: Mouse TRPA1 Reverse: caatgacgcatgc ttctgga	This paper	N/A
Primer: Human GAPDH Forward: cctgcaccaccaa ctgctta	This paper	N/A
Primer: Human GAPDH Reverse: ggccatccacagt cttctgag	This paper	N/A
Recombinant DNA		
pIRES2-EGFP	Addgene	Cat#6029-1
pIRES2-mouse TRPA1-EGFP	This paper	N/A
pIRES2-mouse TRPC1-EGFP	This paper	N/A
pIRES2-mouse TRPV4-EGFP	This paper	N/A
pIRES2-mouse Piezo1-EGFP	This paper	N/A
pSico	Addgene	Cat#11578
pSicoR	Addgene	Cat#11579
pSicoR-Control-shRNA-GFP	This paper	N/A
pSicoR-TRPA1-shRNA-GFP	This paper	N/A
pSicoR-Best1-shRNA-GFP	This paper	N/A
pCINeo-GluR1-L497Y	[45]	N/A
pEGFP-N1	Clontech	Cat#6085-1
Software and Algorithms		
GraphPad Prism 7	GraphPad software	https://www.graphpad.com/scientific-software/prism/; RRID: SCR_015807
MATLAB (R2011b)	Mathworks	http://www.mathworks.com/products/matlab/; RRID: SCR_001622
Imaging WorkBench 6.2	Indec BioSystems	http://www.indecbiosystems.com/imagingworkbench/default.asp; RRID: SCR_016589
pClamp 10.4 (Clampex 10.4, AxoScope 10.4, Clampfit 10.4)	Molecular Devices	http://www.moleculardevices.com/products/software/pclamp.html; RRID: SCR_011323
ImageJ	NIH	https://imagej.nih.gov/ij/; RRID: SCR_003070
Mathematica 11	Wolfram	https://www.wolfram.com/mathematica/; RRID:SCR_014448
Abaqus 2018	Dassault Systemes	https://www.3ds.com/products-services/simulia/products/abaqus/

LEAD CONTACT AND MATERIALS AVAILABILITY

This study did not generate new unique reagents. Further information and requests for resources and reagents should be directed to and will be fulfilled by the Lead Contact, C. Justin Lee (cjl@ibs.re.kr).

EXPERIMENTAL MODEL AND SUBJECT DETAILS

Animals and housing

TRPA1 knockout (KO; B6;129P-Trpa1^{tm1Kykw}/J, RRID: IMSR_JAX:006401) mice were purchased from Jackson Laboratory and genotyped as previously described [20]. They were backcrossed with C57BL/6J mice (RRID: IMSR_JAX:000664) for more than 10 generations and were thought as congenic to C57BL/6J. Best1 KO (Best1^{tm1Lmar}/Best1^{tm1Lmar}, RRID: MGI:3797408) mice in genetic background of BALB/c were used [78]. Both types of mice were maintained as heterozygotes and crossed to obtain null mutants and wild-type (WT) littermates. hGFAP-GFP transgenic mice (RRID: IMSR_JAX:003257) were purchased from Jackson Laboratory. All mice were kept on a 12 h light-dark cycle in a specific-pathogen-free facility with controlled temperature and humidity and had free access to food and water. For *in vivo* tail movement test, 7 to 8-week-old male mice were used. All experimental procedures were conducted according to protocols approved by the directives of the Institutional Animal Care and Use Committee of Korea Institute of Science and Technology (KIST, Seoul, Korea).

Organotypic hippocampal slice culture preparation

Organotypic hippocampal slice culture preparation was performed according to the previous report [9]. Immediately following decapitation, the brains of 7-day-old Sprague-Dawley rats (DBL, Eumseong, Korea) were removed and soaked in ice cold HBSS (#14025126, Thermo) with 20 mM HEPES. The frontal cortex and cerebellum were excised, and the hippocampi were isolated and chopped every 350 μm. Each slice was placed onto a 4.0 μm polytetrafluoroethylene membrane insert (Millicell-CM; Millipore Co, Darmstadt, Germany) in a six-well plate with 1 mL 50% minimum essential medium (#LM007-60, Welgene Inc, Gyeongsan, Korea), 25% horse serum (#S104-01, Welgene Inc, Gyeongsan, Korea), 25% HBSS, 6 g/L D-glucose, 1 mM L-glutamine, 20 mM HEPES, and 1% penicillin-streptomycin (#15140-122, GIBCO) titrated to pH 7.1 with NaOH and HCl. The medium was changed every second day, and cultured slices, incubated at 37°C in a humidified 5% CO_2 incubator, were used after 14 days. All experimental protocols were reviewed and approved by the Institutional Animal Care and Use Committee of Kyung Hee University (KHUASP[SE]-15-024).

HEK293T and HEK293T-Piezo1 knockout (HEK-P1KO) cell culture

Human embryonic kidney 293T (HEK293T) cells were purchased from ATCC (RRID: CVCL_0063) and have been tested for mycoplasma contamination. HEK-P1KO cells (Clone 5E3) were kindly provided by Dr. Patapoutian in the Scripps Research Institute. HEK293T and HEK-P1KO cells were cultured in DMEM (#10-013, Corning) supplemented with 25 glucose, 4 L-glutamine, 1 sodium pyruvate (in mM), 10% heat-inactivated fetal bovine serum (#10082-147, GIBCO) and 10,000 units/ml penicillin–streptomycin (#15140-122, GIBCO). Cells were maintained at 37°C in a humidified 5% CO_2 incubator. 18 h before experimental day, cells were transfected with DNA by transfection reagent (Effectene; #301425, QIAGEN). On experiment day, the transfected cells were replated onto cover-glass for Ca^{2+} imaging and electrophysiological recordings.

Primary mouse astrocyte culture

Primary cultured astrocytes were prepared from cortex of C57BL/6J mouse pups (P0-P2) as described [45]. The cerebral cortex was dissected from the brain and adherent meninges were removed, minced and dissociated into single cell suspension by trituration. Cells were cultured in Dulbecco's modified Eagle's medium (DMEM; #10-013, Corning) supplemented with 25 glucose, 4 L-glutamine, 1 sodium pyruvate (in mM), 10% heat-inactivated horse serum (#26050-088, GIBCO), 10% heat-inactivated fetal bovine serum (#10082-147, GIBCO) and 10,000 units/ml penicillin–streptomycin (#15140-122, GIBCO). Cultures were maintained at 37°C in a humidified 5% CO_2 incubator. On 3 days *in vitro* (DIV), cells were vigorously washed with repeated pipetting and the media was replaced to get rid of debris and other floating cell types. During maintaining the culture before use, the media was replaced every 3-4 days. For gene-silencing experiments with primary cultured astrocytes, various shRNAs were electroporated (Neon Transfection system kit; #MPK10096, Invitrogen) into trypsinized cultured astrocytes 4 days before experimental day and replated onto culture dish. One day before the experimental day, cells were replated onto cover-glass coated with 0.1 mg/ml poly D-lysine (PDL, #P6407, Sigma-Aldrich).

Astrocyte-neuron coculture

For astrocyte-neuron coculture, primary mouse neuron culture was prepared as followed. Embryos from pregnant C57BL/6J mice (E18.5) were decapitated and the cortices were dissected out and were treated with 2.5% trypsin (#15090-046, GIBCO). Dissociated cells were seeded onto 12 mm cover-glass coated with PDL. Cells were cultured in plating medium consisting of neurobasal media supplemented with 5% heat-inactivated fetal bovine serum (#10082-147, GIBCO), 2% B27-supplement (#17504-044, GIBCO), 2 mM Glutamax-I (#35050-061, Thermo) and 10,000 units/ml penicillin-streptomycin (#15140-122, GIBCO). After 7-10 days in culture, primary cultured astrocytes from WT or TRPA1 KO mice were plated on top of the cultured cortical neurons. Astrocytes and neurons on coculture were used for Ca^{2+} imaging after 2-3 days.

METHOD DETAILS

Tail movement test with ultrasound

Tail movement test with ultrasound was performed according to previous report [79]. Ultrasound was produced by two function generators connected in series, in which the first function generator (AGF3022B, Tektronix, Oregon, USA) triggered the operation of the second function generator (33210A, Agilent, CA, USA). The bursts of pulsed sine waves generated from function generators were amplified by the linear power amplifier (AG 1021, T&C Power Conversion, Inc. NY, USA) and then provided a single-element focused ultrasound transducer (EofE Ultrasonics Co., Ltd, Gyenggi-do, Korea) with a diameter of 6.5 cm, a geometrical focal length of 7 cm. Ultrasound was induced with following parameters: 350 kHz fundamental frequency, 1.5 kHz pulse repetition frequency, 0.23 ms pulse duration, 66.67 ms sonication duration. A custom-made, cone-shaped plastic housing was combined with the ultrasound transducer and filled with degassed water for transmitting acoustic waves. The distal end of the housing was sealed with a silicone membrane. TRPA1 KO and Best1 KO mice (male, 8-10 weeks old) were anesthetized by an intraperitoneal (i.p.) injection of ketamine (50 mg/kg body weight; Ketamine, Yuhan Co., Seoul, Korea) and xylazine (5 mg/kg body weight; Rompun, Bayer Korea, Seoul, Korea) mixture. Mouse was positioned on a stereotaxic apparatus (David Kopf Instruments, CA, USA) and lifted by 40 mm to rest the tail on the floor. The ultrasound transducer was affixed above the mouse head, and the focus of the transducer was positioned to target the area of motor cortex. The stimulation location was first selected approximately 3.5 mm lateral to the midline and 7.5 mm posterior to

the rear corner of the mouse's eyes [80]. Once the motor response was elicited, stimulation location was then carefully adjusted to achieve the most sensitive site for inducing motor response in each mouse. Motor responses were quantified as a robustness score of tail movement, which can be easily detected through visual inspection. The scores were ranked from one to three, which was modified from a previous report [31]. A score of one was considered when the tail was twitched but did not leave the surface of the floor. A score of two was assigned less than 1 cm height of tail movement. More than 1 cm height of tail movement was designated as a score of three.

Multielectrode array recording of LILFU-induced neuronal firing

Multielectrode array (MEA) recording was performed according to the previous report [9]. The 8 × 8 MEA (Multi Channel Systems GmbH, Reutlingen, Germany) included an amplifier, four-channel stimulus generator and two temperature-control units maintaining solution and baseplate at 33 °C within 0.01 °C [81]. The MEA was bathed for 1 h in 2% ultrasonol 7 (Carl Roth GmbH, Karlsruhe, Germany), brushed, coated with 0.1% polyethylenimine (PEI; Sigma-Aldrich), and sterilized by UV for at least 3 h. Between experiments, probes were cleaned with 2% ultrasonol 7 in distilled water for 30 min, then rinsed and kept in room-temperature distilled water. Rat brain slices were presoaked in artificial cerebrospinal fluid (ACSF) contained 124 NaCl, 26 $NaHCO_3$, 10 glucose, 3 KCl, 2 $CaCl_2$, 1 $MgCl_2$, 10 HEPES (in mM), adjusted to pH 7.4, and centered on the MEA perfused with 3 ml/min flowing ACSF. Slices were stabilized for 1 h at 33 °C. Slice and MEA array were transferred onto an MEA1060 amplifier interface (1,200 dB gain) and grounded with an Ag/AgCl pellet. Sixty channels of data were sampled at 25 kHz and processed in MC_Rack and MC_Data Tool (Multi Channel Systems, GmbH, Reutlingen, Germany) by desktop computer. For generating LILFU for MEA recording, ultrasound pulser (MKPR-1025; MKC Korea, Seoul, Korea) and water-immersion transducer (10 × 10 mm square crystal element; TKS Co., Busan, Korea) centered approximately 5 mm over the MEA in contact with the perfusing ACSF were used. Ultrasound was induced with following parameters: 500 kHz fundamental frequency, 1.16 kHz pulse repetition frequency, 20.97 μs pulse duration. Parameters were optimized to yield a spatial peak pressure of 11.52 kPa. MEA signals were detected and analyzed as previously described [9]. For all MEA recoding, LILFU was applied for 3 min, following a 3 min baseline. The percent of neuronal firing from the baseline was measured by the number of neuronal firing during 3 min LILFU as a percent of 3 min baseline before LILFU. For blocking experiment, HC030031 (40 μM, #H4415, Sigma-Aldrich), niflumic acid (100 μM, #N0630, Sigma-Aldrich), NPPB (5-Nitro-2-(3-phenylpropylamino)benzoic acid; 100 μM, #N4779, Sigma-Aldrich), AP-5 (50 μM, #0106, Tocris) or kynuranic acid (300 μM, #K3375, Sigma-Aldrich) was put into the ACSF.

Micromachined ultrasound transducer array for *in vitro* Ca^{2+} imaging

Micromachined ultrasound transducer array for *in vitro* Ca^{2+} imaging upon LILFU was fabricated according to the previous report [34]. A piezoelectric micromachined ultrasonic transducer (pMUT) array using a bulk piezoelectric (PZT) film coated with CuNi electrodes on both sides (PIC 151, PI, Germany) was fabricated. The fabrication process starts with a 4-inch silicon-on-insulator (SOI) wafer and the wafer is bonded with a 1-mm-thick bulk PZT film. As a bonding layer between SOI wafer and bulk PZT film, CYTOP (CTL-809; AGC, Japan) is spin-coated on both sides of the SOI wafer and the PZT film. Then, they are bonded together in a wafer-level bonder at the temperature of 160°C with an applied pressure of 3.5 $kg \cdot f/cm^2$. Next, the bonded PZT film is thinned down to 40 μm by chemical mechanical polishing (CMP) process. Then, 300-nm-thick platinum and 20-nm-thick chrome layers are deposited using a sputter and patterned by lift-off process to form top electrodes. To pattern the bulk PZT layer, combination of 150-nm-thick chrome layer and a 10-μm-thick AZ 9260 photoresist layer as an etch mask was used. The PZT layer is etched in a mixture of H_2O:HCl:HF with a ratio of 250:10:1 until the bottom electrode is exposed. After the bottom electrodes are exposed by the PZT etching process, a 300-nm-thick gold and 20-nm-thick chrome adhesion layers are deposited and patterned using lift-off process to provide electrical connections between bottom electrodes and pads. Next, a 100-nm-thick aluminum layer is deposited and patterned on the backside of the SOI wafer as an etch mask for DRIE process. Finally, the membrane of the transducer is released by DRIE process by using the 0.7-μm-thick buried oxide layer as an etch stop layer. The top electrodes are isolated while the bottom electrodes are connected through the silicon substrate to allow for individual control of each element. The fabricated pMUT array was mounted on a printed circuit board (PCB) and pads on the pMUT array were connected to the pads on the PCB using wire bonding. The diameter of the single ultrasound transducer is 500 μm, and the resonant frequency of the transducer was measured to be 430 kHz. The acoustic power from a single transducer can be controlled from 10.2 kPa to 67.3 kPa with varying the applied actuation voltage from 11V to 66 V. In the experiment for Ca^{2+} imaging *in vitro*, ultrasound was induced with following parameters: 430 kHz fundamental frequency, 2 kHz pulse repetition frequency, 0.25 ms pulse duration, 100 ms sonication duration, acoustic power of 67.3 kPa with an applied voltage of 66 V.

TRP gene cloning and shRNA vector construction

Each cDNA encoding full-length mouse TRPA1 (NM_177781.5), mouse TRPC1 (NM_011643.3), mouse TRPV4 (NM_022017.3), or mouse Piezo1 (NM_001357349.1) were subcloned into pIRES2-EGFP vectors (#6029-1, Addgene) by using XhoI and BamH1 sites. The mouse TRPA1 nucleotide (NM_177781.5) from 1767 to 1787 (5′-gcaagcttcctttctgcatat-3′) and the mouse Best1 nucleotides (NM_011913.2) from 774 to 793 (5′-tttgccaacttgtcaatgaa-3′) were selected for the target sequence of each TRPA1- and Best1-shRNA. For making shRNA, two kinds of oligos were purchased (Sequence of oligos; [phos]5′-t [sense sequence of target] ttcaagaga [reverse complement sequence of target] ttttttc-3′ and [phos]5′-tcgagaaaaaa [sense sequence of target] tctcttgaa [reverse complement sequence of target] a-3′). Two oligos were annealed with annealing buffer containing 200 potassium acetate, 60 HEPES-KOH,

4 Mg-acetate (in mM), adjusted pH 7.3 by KOH and incubated at 95°C for 5 min and 70°C for 10 min. The annealed double-stranded oligo was inserted into SacII-NotI rescticion sites of pSico (#11578, Addgene) or HpaI-XhoI restriction enzyme sites of pSicoR lentiviral vector (#11579, Addgene) [55] and verified by sequencing.

Ca^{2+} imaging

Cells (HEK293T, HEK-P1KO, astrocyte or astrocyte-neuron coculture) were incubated with 5 μM Fura-2 AM (#F1201, Thermo Fisher Scientific) mixed with 1 mL of external solution containing 5 μL of 20% pluronic acid (#P3000MP, Thermo Fisher Scientific) for 40 min at room temperature. External solution contained 150 NaCl, 10 HEPES, 3 KCl, 2 $CaCl_2$, 2 $MgCl_2$, 5.5 glucose (in mM), adjusted to pH 7.3 and osmolarity to 325 mOsmol kg^{-1}. Intensity images of 510 nm wavelength were taken at 340 nm and 380 nm excitation wavelengths using either iXon EMCCD (DV887 DCS-BV, ANDOR technology, Belfast, UK). The two resulting images were acquired in Axon Imaging Workbench 6.2 (Indec BioSystems, CA, USA) and analyzed in Clampfit 10.4 (Molecular Devices, CA, USA). For Ca^{2+} imaging in TRPA1, TRPC1, TRPV4 or Piezo1-transfected HEK293T, each DNA construct was transfected into HEK293T using Effectene transfection reagent (#301425, QIAGEN). The number of cells showing Ca^{2+} response during 3 min LILFU was calculated as a percent of responsive cells. The threshold of Ca^{2+} response was determined by unimodal thresholding [82] calculated by MATLAB (R2010b, Mathworks). The Ca^{2+} peak amplitude (ratio) in Ca^{2+} imaging upon LILFU was measured during 3 min LILFU. Onset time of Ca^{2+} response in experiment with astrocyte-neuron coculture (Figures 3D–3F) was measured during 5 min after the start time of LILFU. The Ca^{2+} peak amplitude (ratio) in Ca^{2+} imaging upon NMM - (Figures S4C, S4F, and S5C) or poking- (Figure S5I) was measured after the time of NMM treatment or poking. For blocking experiment, 40 μM HC030031 (#H4415, Sigma-Aldrich) or 50 μM AP-5 (#0106, Tocris) was put into the external solution. For positive control of TRPA1, 100 μM NMM (*N*-Methylmaleimide; #389412, Sigma-Aldrich) was put into the external solution. For depletion of the endoplasmic reticulum Ca^{2+}, 1 μM thapsigargin (#T9033, Sigma-Aldrich) was put into the external solution.

Indentation (Piezo-electrically driven mechanical stimulation)

Piezo-electrically driven mechanical stimulation was achieved as previously described [38, 39]. A fire-polished glass electrode (tip diameter: 3 ~4 μm) as a probe was positioned at an angle of 50° to the cell surface. Downward movement of the probe was controlled by a micromanipulator (Nano-controller NC4; Kleindiek Nanotechnik, Germany) connected with computer. The initial position of the probe on the cell surface was determined by looking at the indentation of the cell surface through a microscope. Then, 1.0 μm of indentation was delivered to the cell surface, which was considered as the initial point of piezo-electrically driven mechanical stimulation. From the initial position, the mechanical steps were made by moving the probe downward up to 5 μm in 2 μm increments. The duration of the piezo-electrically driven mechanical stimulation was 600 ms.

Poking

Poking was achieved using poking pipette (4 ~7 MΩ) filled with HEPES buffer contained 150 NaCl, 10 HEPES, 3 KCl, 2 $CaCl_2$, 2 $MgCl_2$, 5.5 glucose (in mM), adjusted to pH 7.3 and osmolarity to 325 mOsmol kg^{-1}. For measuring resistance of poking pipette, Digidata 1322A (Axon Instruments), Axopatch 200A amplifier (Axon Instruments) and pClamp 10.4 software (Molecular Devices) were used. Cultured astrocyte or HEK293T or HEK-P1KO were monitored by iXon EMCCD (DV887 DCS-BV, ANDOR technology, Belfast, UK). We recorded not only the resistance of poking pipette determined by the current generated by periodic test pulses of 10 mV at 20 Hz using Clampex 10.4 (Molecular Devices), but also the indentation depth displayed by the MPC-200 micromanipulator (Sutter Instrument) which has 0.0625 μm resolution. We first moved the poking pipette to the cell membrane manually using MPC-200 micromanipulator very slowly. When the poking pipette touched the cell membrane, which was the initial point of stimulation, the resistance of poking pipette started to increase. We then slowly lowered the poking pipette until its resistance increase (ΔR) reached 3 ~6 MΩ within 20 ~30 s for HEK293T and HEK-P1KO or 0.2 ~0.5 MΩ within 3 ~5 s for astrocyte, until a large inward current was induced. Finally, we raised the poking pipette from the cell membrane slowly within 5 ~10 s. After finishing the recording, the exact ΔR value was calculated from the recorded current amplitude of poking pipette.

Whole-cell patch-clamp recording

For fast-exerted indentation-induced current recording, whole-cell patch-clamp recording was performed as previously described [39]. External solution contained 130 NaCl, 5 KCl, 1 $CaCl_2$, 2 $MgCl_2$, 10 HEPES, 10 D-mannitol (in mM), adjusted to pH 7.2 with NaOH. Currents were recorded from HEK293T or HEK-P1KO under voltage clamp (V_h = −60 mV) using Axopatch 200A amplifier (Axon Instruments), acquired with pClamp 10.4 (Molecular Devices). Recording pipette (2 ~3 MΩ) was filled with 130 CsCl, 2 $MgCl_2$, 10 HEPES, 2 Mg-ATP, 0.2 Na_3-GTP, 25 D-mannitol (in mM), adjusted to pH 7.2 with CsOH. Current amplitude at the peak or 600 ms after indentation was measured. For poking-induced current recording, whole-cell patch-clamp recording was performed. External solution contained 150 NaCl, 10 HEPES, 3 KCl, 2 $CaCl_2$, 2 $MgCl_2$, 5.5 glucose (in mM), adjusted to pH 7.3 and osmolarity to 325 mOsmol kg^{-1}. Currents were recorded from cultured astrocytes or HEK293T or HEK-P1KO under voltage clamp (V_h = −70 mV) using Axopatch 200A amplifier (Axon Instruments), acquired with pClamp 10.4 (Molecular Devices). Recording pipette (4 ~7 MΩ) was filled with 110 Cs-gluconate, 30 CsCl, 0.5 $CaCl_2$, 10 HEPES, 4 Mg-ATP, 0.3 Na_3-GTP and 10 BAPTA (in mM), adjusted to pH 7.3 with CsOH and osmolality to 290-310 mOsmol kg^{-1} with sucrose. For comparing the poking-induced current, the current amplitude was measured 5 s after time of poking and analyzed by Clampfit 10.4 (Molecular Devices). For H_2O_2 scavenger experiment, edaravone (MCI-186; 10 μM, #ab120645, Abcam) or AAD-2004 (10 μM, GNT Pharma) was put into external solution.

Cell-attached patch-clamp recording with negative pressure

For single channel current recording with negative pressure, cell-attached patch-clamp recording was performed as previously described [40]. External solution contained 140 KCl, 10 HEPES, 1 $MgCl_2$, 10 glucose (in mM), adjusted to pH 7.3 with KOH. Currents were recorded from cultured astrocytes or HEK293T or HEK-P1KO under voltage clamp (V_h = −80 mV) using Axopatch 200A amplifier (Axon Instruments), acquired with pClamp 10.4 (Molecular Devices). Recording pipette (4 ~7 MΩ) was filled with 130 NaCl, 5 KCl, 10 HEPES, 1 $CaCl_2$, 1 $MgCl_2$, 10 TEA-Cl, adjusted to pH 7.3 with NaOH. Negative pressure steps (0 ~-60 mmHg, Δ10 mmHg) were exerted via the recording electrode using pressure clamp HSPC-1 device (ALA Scientific Instruments, NY, USA) controlled by Clampex 10.4 (Molecular Devices). The duration of the negative pressure was 500 ms. Current amplitude and open probability (Po) was measured by Clampfit 10.4 (Molecular Devices) after recording. For blocking TRPA1, 40 μM HC030031 (#H4415, Sigma-Aldrich) was put into the internal solution of recording pipette.

Sniffer-patch from primary cultured cortical astrocytes

Primary cortical astrocytes were prepared from postnatal day P0 ~P2 of C57BL/6J mice (RRID: IMSR_JAX:000664). One day before the experiment, HEK293T were transfected with 1:10 ratio of pEGFP-N1 (#6085-1, Clontech) and GluR1-L497Y receptor [45] using Effectene (#301425, QIAGEN). 50 μM CNQX (#0190, Tocris) was always supplemented in the medium to block the AMPA receptor-mediated cytotoxicity. On the day of sniffer-patch, HEK293T expressing GluR1-L497Y were dissociated, triturated, added onto the cover-glass with cultured astrocytes, and then allowed to settle for at least 1 h before sniffer-patching. 50 μM CNQX was also added to the mixed culture of astrocyte and HEK293T to block the AMPA receptor-mediated cytotoxicity. After HEK293T settled, cultured astrocytes were incubated with 5 mM Fura-2AM (#F1201, Thermo Fisher Scientific) for 40 min and washed at room temperature and subsequently transferred to a microscope stage. External solution contained 150 NaCl, 10 HEPES, 3 KCl, 2 $CaCl_2$, 2 $MgCl_2$, 5.5 glucose (in mM), adjusted to pH 7.3 and osmolarity to 325 mOsmol kg^{-1}. Intensity images of 510 nm wavelength were taken at 340 nm and 380 nm excitation wavelengths using iXon EMCCD (DV887 DCS-BV, ANDOR technology, Belfast, UK). The two resulting images were used for ratio calculations in Axon Imaging Workbench 6.2 (Indec BioSystems). GluR1-L497Y-mediated currents were recorded from HEK293T under voltage clamp (V_h = −70 mV) using Axopatch 200A amplifier (Axon Instruments), acquired with pClamp 10.4 (Molecular Devices). Recording pipette (4 ~7 MΩ) was filled with 110 Cs-gluconate, 30 CsCl, 0.5 $CaCl_2$, 10 HEPES, 4 Mg-ATP, 0.3 Na_3-GTP and 10 BAPTA (in mM), adjusted to pH 7.3 with CsOH and osmolality to 290-310 mOsmol kg^{-1} with sucrose. To normalize different amounts of expression of GluR1-L497Y on the HEK293T, 1 mM of glutamate in the bath was applied to maximally activate the GluR1-L497Y after current recording. Normalization was then accomplished by dividing the current induced by glutamate from astrocytes by the current induced by bath application of glutamate. The Ca^{2+} peak amplitude (ratio) from astrocytes and peak current amplitude from sensor cells were measured after the time of poking and analyzed by Clampfit 10.4 (Molecular Devices).

Computational simulation for LILFU- and poking-induced pressure distribution on the surface of astrocyte

According to d'Alembert's wave equation, the propagation of ultrasonic wave can be described by a second-order partial differential equation

$$\frac{\partial^2 \psi}{\partial t^2} = v^2 \nabla^2 \psi$$

where v is the speed of sound and the displacement ψ is a function of position $\vec{r}$ and time t. The Laplacian of ψ in isotropic space is simplified to

$$\nabla^2 \psi = \frac{1}{r^2} \frac{\partial}{\partial r} \left(r^2 \frac{\partial \psi}{\partial r} \right)$$

where $r = |\vec{r}|$, then the partial differential equation can be expressed by

$$\frac{\partial^2 (r\psi)}{\partial t^2} = v^2 \frac{\partial^2 (r\psi)}{\partial r^2}$$

and one can obtain the harmonic solution of the equation as

$$\psi(\vec{r}, t) = \frac{\psi_0}{r} \cos(2\pi f t - kr + \phi)$$

with a given frequency f and a phase ϕ where ψ_0 is a constant and k the wave number defined by $2\pi f/v$, which shows a wave generated by a point source located at the origin. By the principle of superposition one can assume that the waves generated by point sources located at arbitrary positions can be the sum of the waves that would have been caused by each stimulus individually. Therefore, we can obtain a function describing a wave generated by an arbitrary shaped sound source. We have calculated the sound pressure in the area with a diameter of 100 μm to mimic a typical membrane surface of an astrocyte. The area is 1 mm apart from a circular ultrasonic transducer with a diameter of 500 μm. We have stimulated point sources located in the transducer area with the binary phases of 0 and π, which are associated to point sources in arbitrary manner. The result of simulation is obtained by using Mathematica 11 (Wolfram, USA) as the 3 dimensional pressure distribution on the membrane surface of astrocyte.

The simulation of the mechanical poking onto the surface of an astrocyte is accomplished by pressing a shell structure with a diameter of 100 μm to mimic an astrocyte, by the tip of a rounded rod. The starting geometry of the shell structure is similar to a disk with rounded edges and with a negative gradient from the center to the border in the case of the top surface. The height of the disk is set to 1.5 μm. The rod moves down, according to the central normal axis to the top surface of the shell structure, to the half of the central thickness. The elastic modulus of the shell surface is set to 60 kPa, based on the atomic force microscopic measurement from astrocytes [50]. The pressure distribution on the surface of the shell structure was calculated and displayed by Abaqus 2018 (Dassault Systemes, France).

Electron microscopy

For electron microscopic immunostaining for GFP and TRPA1, three hGFAP-GFP transgenic mice (male, 8-10 weeks old; RRID: IMSR_JAX:003257) were deeply anesthetized with sodium pentobarbital (80 mg/kg, i.p. injection) and perfused transcardially with 10 mL heparinized normal saline followed by 50 mL freshly prepared mixture of 4% paraformaldehyde and 0.01% glutaraldehyde in 0.1 M phosphate buffer, pH 7.4. Hippocampus was removed and postfixed in the same fixative for 2 h at 4°C. Sections were cut sagittally on a Vibratome at 60 μm and cryoprotected in 30% sucrose in PB overnight at 4°C. Next day, sections were frozen on dry ice for 20 min, thawed in phosphate-buffered saline (PBS; 0.01 M, pH 7.4) to enhance penetration. They were pretreated with 1% sodium borohydride for 30 min to quench glutaraldehyde and then blocked with 3% H_2O_2 for 10 min to suppress endogenous peroxidases and with 10% normal donkey serum (Jackson ImmunoResearch, PA, USA) for 30 min. For double immunostaining for GFP and TRPA1, sections of hippocampus were incubated overnight in a mixture of chicken anti-GFP (1:300, #GFP-1020, Aves Labs, Oregon, USA) and rabbit anti-TRPA1 [83] (1:80, kindly donated from Prof. Noguchi, Hyogo college of medicine, Japan) antibodies. After rinsing in PBS, sections were incubated with a mixture of biotinylated donkey anti-chicken (1:200, #703-065-155, Jackson ImmunoResearch) and 1 nm gold-conjugated donkey anti-rabbit (1:50, #25701, EMS, PA, USA) antibodies for 2 h. The sections were postfixed with 1% glutaraldehyde in PB for 10 min, rinsed in PB several times, incubated for 4 min with HQ silver enhancement solution (Nanoprobes, NY, USA), and rinsed in 0.1 M sodium acetate and PB. The sections were then incubated with ExtrAvidin peroxidase (1:5,000, Sigma-Aldrich) for 1 h and the immunoperoxidase was visualized by nickel-intensified 3,3′-diaminobenzidine tetrahydrochloride (DAB). Sections were further rinsed in PB, osmicated (in 0.5% osmium tetroxide in PB) for 1 h, dehydrated in graded alcohols, flat-embedded in Durcupan ACM (Fluka, Buchs, Switzerland) between strips of Aclar plastic film (EMS), and cured for 48 h at 60°C. Chips containing prominent staining for GFP and TRPA1 in the hippocampus were cut out of the wafers and glued onto blank resin blocks with cyanoacrylate. Serially cut thin sections were collected on Formvar-coated single-slot nickel grids and stained with uranyl acetate and lead citrate. Grids were examined on a Hitachi H 7500 electron microscope (Hitachi, Tokyo, Japan) at 80 kV accelerating voltage. Images were captured with Digital Montage software driving a MultiScan cooled CCD camera (ES1000W, Gatan, CA, USA) attached to the microscope. To control specificity of primary antibodies, sections of CA1 were processed according to the above-described protocols, except that primary or secondary antibodies were omitted. Omission of primary or secondary antibodies completely abolished specific staining. In addition, specificity of the immunoreaction was also confirmed by the consistency of immunostaining in adjacent serial thin sections of the same astrocytes. For quantitative analysis of TRPA1 expression in different compartment of astrocyte (soma, process, and microdomain), thirty electron micrographs at 25,000 X were taken of all $TRPA1^+/GFP^+$ astrocyte within 939 μm^2 from one thin sections in each hippocampal CA1 of three mice. Small astrocytic process that is smaller than 0.3 μm in diameter was defined as microdomain. Gold particle that is at the plasma membrane and within 25 nm from it was defined as membrane-bound gold particle. The density of gold particle for TRPA1 was determined by manual counting of gold particles over the area of GFP^+ profiles: cell nuclei and mitochondria were excluded.

Evaluation of mouse skull effect on ultrasound transmission

Ex vivo mouse skulls were isolated to evaluate the attenuation of ultrasound transmission by measuring acoustic pressure (Figure S1B). The pressure distribution field was measured in a degassed water tank using a calibrated needle-type hydrophone (HNR-500, Onda Corporation, CA, USA) attached to a three-axis robotic platform (Bi-Slides, Velmex, NY, USA) moving with 0.5 mm intervals. The skull was located on the end of the transducer housing, and the hydrophone tip was located parallel to the beam axis with the tip at the geometrical focus of the transducer. The spatial-peak temporal-average intensity was calculated by using the formula in previous report [84].

Quantitative real-time PCR

Gene silencing with shRNA targeting TRPA1 was tested by quantitative real-time PCR (qRT-PCR). HEK293T were transfected with 1:1 ratio of TRPA1-shRNA tagging with mCherry and TRPA1 tagging with GFP using Effectene transfection reagent (#301425, QIAGEN). Approximately 3 days after transfection, total RNA was extracted by using RNA isolation kit (RNeasy Mini Kit, #74104, QIAGEN). cDNA was synthesized by using reverse transcriptase (SuperScript III reverse transcriptase; #18080-044, Invitrogen). For qRT-PCR, SYBR-green (SYBR Green PCR master mix; #4309155, Applied Biosystems) was used. The following sequences of primers were used for quantitative real-time PCR. Mouse TRPA1 forward: 5′-gcatacccagtcctgacctt-3′; Mouse TRPA1 reverse: 5′-caatgacgcatgcttctgga-3′. Human GAPDH forward: 5′-cctgcaccaccaactgctta-3′; Human GAPDH reverse: 5′-ggccatccacagtctt ctgag-3′.

Western blot

Cultured cortical astrocytes transfected with control- or TRPA1-shRNA were lysed with RIPA buffer (#R4100, GenDEPOT) containing protease inhibitor cocktail (#P3100, GenDEPOT). 40 μg of obtained protein lysates were separated by protein electrophoresis using protein gels (#4561084, BIORAD) and blotted onto PVDF membranes (#1704156, BIORAD). The blots were incubated overnight at 4°C with rabbit anti-TRPA1 (1:500, Abfrontier, Korea) and rabbit anti-actin (1:2000, #A2066, Sigma-Aldrich). Blots were then washed and incubated with horseradish peroxidase-conjugated donkey anti-rabbit IgG (#NA9340, Amersham), followed by washing and detection of immunoreactivity with enhanced chemiluminescence (GE Healthcare Life Sciences). The band intensity was acquired by ImageQuant LAS 4000 (GE Healthcare) and quantified using ImageJ software (NIH).

QUANTIFICATION AND STATISTICAL ANALYSIS

Data are presented as mean ± SEM. For all experiments, data normality was analyzed using a D'Agostino–Pearson omnibus normality test. Differences between groups were evaluated by unpaired two-tailed t test or one-way ANOVA with Tukey's multiple comparisons tests. For data not following normal distribution, a Mann-Whitney test (Two-tailed) or Kruskal–Wallis test with Dunn's multiple comparison test were performed. For tail movement test data, two-way ANOVA with Sidak's multiple comparisons test was performed for statistical analysis. Data from multiple independent experiments was assumed to be normal variance. $p < 0.05$ was considered to indicate statistical significance throughout the study. The significance level is represented as asterisks (*$p < 0.05$, **$p < 0.01$, ***$p < 0.001$; ns, not significant). Detailed statistical analysis contents are described in Table S1. All data are presented as mean ± SEM. No statistical method was used to predetermine sample size. Sample sizes were determined empirically based on our previous experiences or the review of similar experiments in literatures. The numbers of animals used are described in the corresponding figure legends or on each graph. All experiments were done with at least three biological replicates. Animals were genotyped before experiments, and they were all caged together and treated in the same way. Animals were randomly and evenly allocated to each experimental group. To perform the group allocation in a blinded manner during data collection, animal preparation and experiments were performed by different investigators. No data point was excluded. GraphPad Prism 7.02 for Windows (GraphPad Software) was used for these analyses and to create the plots. Additional statistical details are provided in Table S1.

DATA AND CODE AVAILABILITY

This study did not generate code. Means and SEMs are posted here in Table S1.